A benchmark study on SEM aberration retrieval

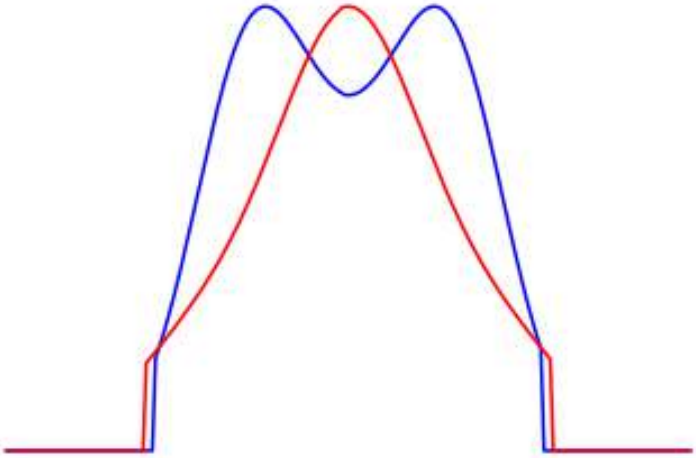

Ruben Dortland

Bachelor End Project
AP/AM Double Bachelor
TU Delft

Delft, July 9, 2024
Supervisors: A.M. Gheidari, K. Vuik
Secondary supervisors: J.L.A. Dubbeldam, I. Zadeh

Preface and acknowledgements

This report is written as the Bachelor End Project of the double bachelor Applied Physics and Applied Mathematics at the TU Delft.

I want to thank all people involved in this project. A couple of names need to be mentioned explicitly. First, I want to thank my supervisors Ali Gheidari and Kees Vuik, for being patient with me, and providing support throughout the entire process of my research and writing of my report. I also want to thank Diederik Maas and Maurice Krielaart for guiding me through the first steps of my project, and Yifeng Shao for providing me with some useful insight into aberrated wavefront simulations. Finally, I want to thank Sarnia Fazlali for helping me with the aberration retrieval code as her initial template for the code helped the process of this research significantly, and Joost Verbaan for providing insightful discussions during the time we were writing our theses at the ImPhys department.

Abstract

This report focuses on the process of aberration coefficient retrieval for measurements of a Scanning Electron Microscope (SEM). The main goal is the verification of a modified aberration coefficient retrieval method described in an article by Uno et al. (2005) [1]. This method first extracts spot profiles, represented by Point Spread Functions (PSFs), from a through-focus series of SEM images using Fourier analysis. The size and shape of a PSF characterize the performance of a SEM. Afterward, it determines characteristics from these PSFs to obtain aberration coefficients.

The process consisted of three parts: probe shape extraction, PSF analysis, and aberration coefficient calculation, which included a consistency test. The original method was changed to include clarification for the use of complex conjugates of functions in the Fourier domain, the proper statistical definition of standard deviation as characteristic of the width of a PSF, the curvature definition used in the method, and contour tracing around a PSF to exclude points outside the contour. These adaptations were made to clarify the methods described in the reference article.

This modified method was tested against generated PSFs that used the wave-optical description of five different aberrations. By increasing the value of these individual simulated aberration coefficients C'_n with factors $s \in [1, S], S \in \mathbb{N}$, the consistency of this retrieval method could be determined by calculating the ratio Q between simulated and retrieved aberration coefficients as a function of the factor s.

The spot shape extraction method was implemented and assessed successfully, as the shapes of the generated PSFs were successfully retrieved, and the use of complex conjugates of functions in the Fourier domain resulted in rotated spot shapes.

Contour tracing around the retrieved PSFs had mixed results. For all aberrations, it presented a good measure of the spot shape. The implementation of an algorithm that excluded points p_j outside the contour was not accurate for one test aberration: two-fold astigmatism A_2. The contour tracing algorithm excludes important parts of the shapes of the PSFs. From research into the characteristics asymmetry μ, width σ, and curvature ρ it could be inferred that the first two characteristics μ and σ represent the mean and standard deviation of discrete probability mass functions. Curvature ρ has no such direct statistical equivalent, it was concluded however that this characteristic presented a good measure for the effect of third-order spherical aberration in a PSF.

Results could not indicate that this wave-optical description of aberrations is consistent with all of the coefficients retrieved using the modified method of aberration coefficient retrieval as the ratio Q remained consistent for defocus C_{df}, three-fold astigmatism A_2 and third-order spherical aberration C_s as a function of the factors s.

Continued research into this method of aberration retrieval is recommended, specifically in the definitions of the characteristic curvature ρ, more advanced contour tracing, and the digitizations of aberration coefficients. More assessment and modification of this method of aberration coefficient retrieval can allow for a more comprehensive understanding of the method, which will eventually contribute to an automatic aberration corrector that could speed up SEM measurements significantly.

Contents

List of Symbols

(X, Y) Spatial frequency coordinates

(x, y) 2D Cartesian coordinates

$\mathcal{F}$ Fourier transform

$\mathcal{F}^{-1}$ Inverse Fourier transform

μ Line profile asymmetry

μ_{Airy} Mean of the Gaussian used to approximate the Airy pattern

ρ Line profile curvature

σ Line profile width

σ_{Airy} Standard deviation of the Gaussian used to approximate the Airy pattern

θ_k Angle of line profile k (rad)

$\vec{v_k}$ Direction vector of line profile k

A_1 First-order astigmatism coefficient (m)

A_2 Second-order astigmatism coefficient (m)

A_3 Third-order astigmatism coefficient (m)

B_2 Second-order coma coefficient (m)

C'_n General notation for a simulated aberration coefficient (m)

C_n General notation for an aberration coefficient (m)

C_s Third-order spherical aberration coefficient (m)

C_{df} Defocus coefficient (m)

d Maximum distance from the centroid to the edge of the cropped image (in pixels)

$F(X, Y)$ Fourier transform of $f(x, y)$

$f(x, y)$ Sample surface

$G(X, Y)$ Fourier transform of $g(x, y)$

$g(x, y)$ Point Spread Function (PSF)

$H(X, Y)$ Fourier transform of $h(x, y)$

$h(x, y)$ Measured image

I Maximum size of an image (in pixels)

M Number of points on one profile line

N Number of profile lines drawn across a PSF

P_{size} Pixel size (m)

$Q(C_n, s)$ Ration between pre-determined aberration coefficients C'_n and retrieved aberration coefficients C_n

r_{Airy} Airy disk radius up to the first zero of the pattern (m)

S Maximum factor $s \in [1, S]$

s Factor $s \in \mathbb{N}$

S_3 Third-order star aberration coefficient (m)

V Field of view depicted in a SEM image (m)

w, l Width and length of the cropped PSF image (in pixels)

Introduction

In classic light optics, there is a physical limit to the resolution of any optical instrument. This is called the Abbe diffraction limit, named after the German physicist who found this limit in 1873 [2]. Consequently, there is a minimum resolvable distance for any optical instrument that uses light for image formation, including light microscopes. Since then, many new methods for microscopy have been developed that can bypass the diffraction limit. However, these new methods bring other complications in technology.
The Electron Microscope is one of these new microscopy methods. As the name suggests, an electron microscope uses electrons to create images like a classic microscope uses light (photons). The wavelength of an electron is much smaller than that of light, which means that the diffraction limit of an electron microscope is also smaller. There are various types of electron microscopes, and in this report, we will focus on the Scanning Electron Microscope [3], SEM for short. Also see figure (1a), which shows a state-of-the-art SEM developed by Hitachi in (1a). The MInT department uses a variant of this microscope.

An SEM scans the surface of a sample with electrons. The electrons originate from an electron source and are passed through various electron lenses and coils in a vacuum that force the electrons into a narrow beam. This beam is focused on the sample with an energy range of 50-30.000 eV, depending on the voltage under which the SEM operates, and it forces secondary electrons on the surface of the sample to scatter in various directions at various intensities. The scattered electrons are then detected by a detector [4], and from there, the detected electrons are imaged in an intensity reading, resulting in a high-resolution image. This process is also illustrated in figure (1b) [3].

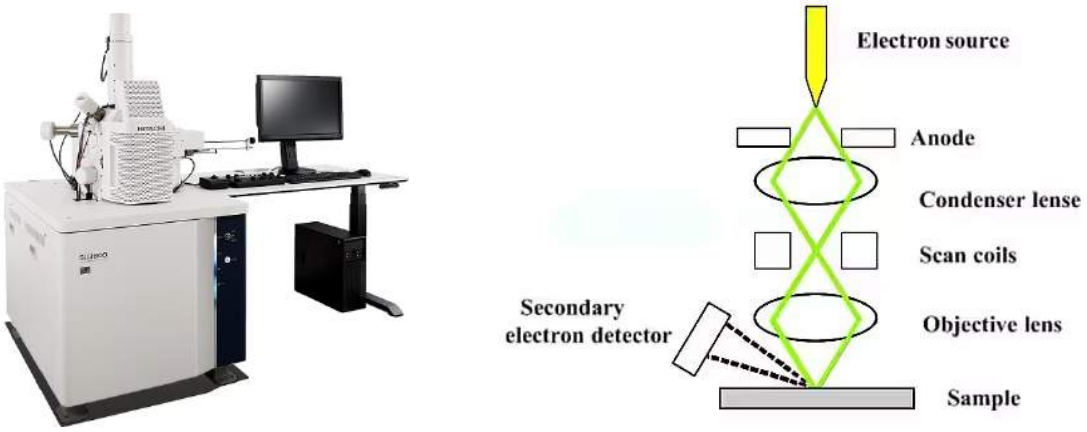

(a) *State of the art SEM, developed by Hitachi* [5]. (b) *Schematic view of an SEM* [3].

Figure 1: *State-of-the-art SEM, developed by Hitachi (left) and a schematic view of a Scanning Electron Microscope (right).*

This high-resolution image is not so easily obtained, however. Many complications reduce the overall quality of the measured image aside from the diffraction limit. One such complication occurs when focusing the electron beam on the sample. If the beam is not perfectly focused on the sample, or if there are imperfections in the lenses or other parts of the microscope, the

beam can get distorted or spread out, lowering the image's resolution. We call the resulting blur and distortion *aberrations*: deviations from the ideal image, which would be obtained with a perfect beam. These aberrations can occur due to various phenomena and are characterized by *aberration coefficients*. Understanding and researching the profile of the spot with which an electron beam in SEM hits a sample, and how the spot changes with an imperfectly focused beam due to aberrations is therefore very important. Extensive research has already been done in both the calculation of aberration coefficients [6], and in the development of aberration correctors [7] [8] [9], where extra components are added to an electron microscope to diminish, or 'cancel out' the effects of aberrations that occur in the optical system. This research will eventually contribute to an automatic aberration corrector, which will speed up measurements with the SEM at the MInT department significantly.

In this report, the main goal is to describe the process of spot profile and aberration coefficient retrieval for SEM imaging systems. This is accomplished by first calculating and extracting the probe shape, represented by the Point Spread Function (PSF), of an SEM image in under, just, and over focus. From there, using line profiles through the PSFs, the aberration coefficients are calculated. This method is verified using simulated PSFs with five test aberration coefficients C_n of low order by computing the aberration coefficient ratio $Q(C_n)$ between simulated and retrieved coefficients, and seeing if $Q(C_n)$ remains constant. In Chapter 2, the theoretical section of the research is described. Chapter 3 discusses the code used to determine a spot profile and a selected group of aberration coefficients, as well as the test we will use to determine the accuracy of this method. Chapter 4 presents the results of these experiments, and in Chapter 5 we discuss various limitations and complications concerning spot shape retrieval, as well as deviations of the results from measured spot shapes. Finally, we conclude the report in Chapter 6, with presented recommendations.

Theory

Introduction

This chapter contains a concise overview of the theory needed to extract aberration coefficients from a series of SEM images. First, the optical system representing SEM imaging is defined, and from there the definition of the Point Spread Function is given. Secondly, line profiles are introduced and applied to under- and over-focus point spread functions to determine the characteristics of the profiles: width σ, asymmetry μ, and curvature ρ. Lastly, the equations that calculate the aberration coefficients from these characteristics are discussed.

Optical system

The main goal of this project is to visualize and analyze the electron probe of an SEM. The first step is obtaining an expression for this probe. Figure (2) depicts an illustration of the image formation process of an SEM. From the objective lens, a focused primary electron beam lands on a sample. The surface of the sample absorbs these electrons and scatters secondary electrons. The intensity of these secondary electrons is measured by a detector, from which an image is formed. The sample is assumed to be of negligible height (2D). Let $f(x, y)$ denote the

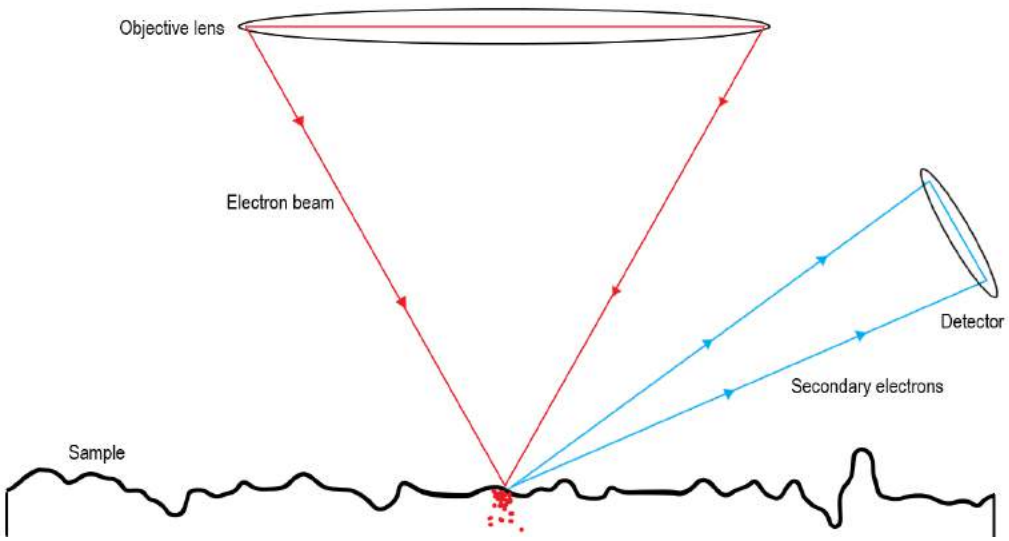

Figure 2: *Schematic view of the image formation of a Scanning Electron Microscope (exaggerated). From the objective lens, a focused primary electron beam (red) lands on the sample. The sample absorbs (red dots) these electrons, and scatters secondary electrons (blue). The intensity of these secondary electrons is measured by a detector, from which an image is formed.*

surface of the sample and $g(x, y)$ the probe intensity profile, or *Point Spread Function* (PSF). The imaging process of an SEM is described as a 2D convolution of the PSF $g(x, y)$ over the sample surface $f(x, y)$ to create an image $h(x, y)$ [10]:

$$h(x, y) = \int_{-\infty}^{\infty} \int_{-\infty}^{\infty} f(u, v) g(u - x, v - y) \, \mathrm{d}u \, \mathrm{d}v + \gamma(x, y), \tag{1}$$

where (x, y) denote the coordinates of a pixel. An additional term $\gamma(x, y)$ representing the noise during an SEM measurement at coordinate (x, y) is added.
Equation (1) can be reformulated in the Fourier domain:

$$H(X, Y) = F(X, Y)G(X, Y) + \Gamma(X, Y). \tag{2}$$

Here (X, Y) denotes the spatial frequency coordinate and H, G, F and Γ are the Fourier transforms $\mathcal{F}$ of their spatial domain functions h, g, f and γ respectively.
For the case $\Gamma = 0$, the complex PSF $g(x, y)$ is obtained from equation (2) by using the inverse Fourier transform $\mathcal{F}^{-1}$:

$$g(x, y) = \mathcal{F}^{-1}[G(X, Y)] = \mathcal{F}^{-1}\left[\frac{H(X, Y)}{F(X, Y)}\right] \tag{3}$$

Probe shape extraction

Consider three SEM images that depict the same sample f. The first is measured with a just-focused probe g. The second g_u and third g_o probes are measured with an under- and overfocused probe respectively. From equation (2) with $\Gamma = 0$, we obtain the following system of equations:

$$\begin{aligned} H(X, Y) &= F(X, Y)G(X, Y), \\ H_{u,o}(X, Y) &= F(X, Y)G_{u,o}(X, Y). \end{aligned} \tag{4}$$

By dividing these functions and rearranging the equation, we get the following expression for the Fourier Transform of the under- and over-focused PSF of the electron probe, also called the *Optical Transfer Function*:

$$G_{u,o}(X, Y) = G(X, Y)\frac{H_{u,o}(X, Y)}{H(X, Y)}. \tag{5}$$

From here, obtaining the complex PSF $g_{u,o}$ is done using the inverse Fourier transform $\mathcal{F}^{-1}$:

$$|g_{u,o}| = |\mathcal{F}^{-1}[G_{u,o}]|, \tag{6}$$

where $|g_{u,o}|$ denotes the modulus of $g_{u,o}$, since a PSF can only be visualized as its modulus in 2D. Equations (5) and (6) give us a template for calculating a defocused probe, when the ideal, just focused probe g is known [1].

Point spread function

The point spread function (PSF) is a function that describes the performance of an optical system. If an imaging system is ideal, the PSF $g(x, y)$ would equal a two-dimensional Dirac-delta function $\delta(x, y)$, such that equation (1) gives $h(x, y) = f(x, y)$. In practice, however, this is not the case. Various factors, such as diffraction, limit the resolution of the image.
To clarify, take the sample surface $f(x, y)$ to be the USAF Test chart of 256 by 256 pixels [11]. After convolving the sample with a PSF of arbitrary size (not equal to the Dirac-delta function), the image becomes slightly blurred. This is illustrated in figure (3a).
The size of the PSF also affects the resulting image. A larger PSF leads to a blurrier image, and a smaller PSF results in a sharper image, see figures (3b) and (3c). The effectiveness of an optical system is often characterized by the size and shape of its PSF, where a smaller PSF indicates a better-performing system.

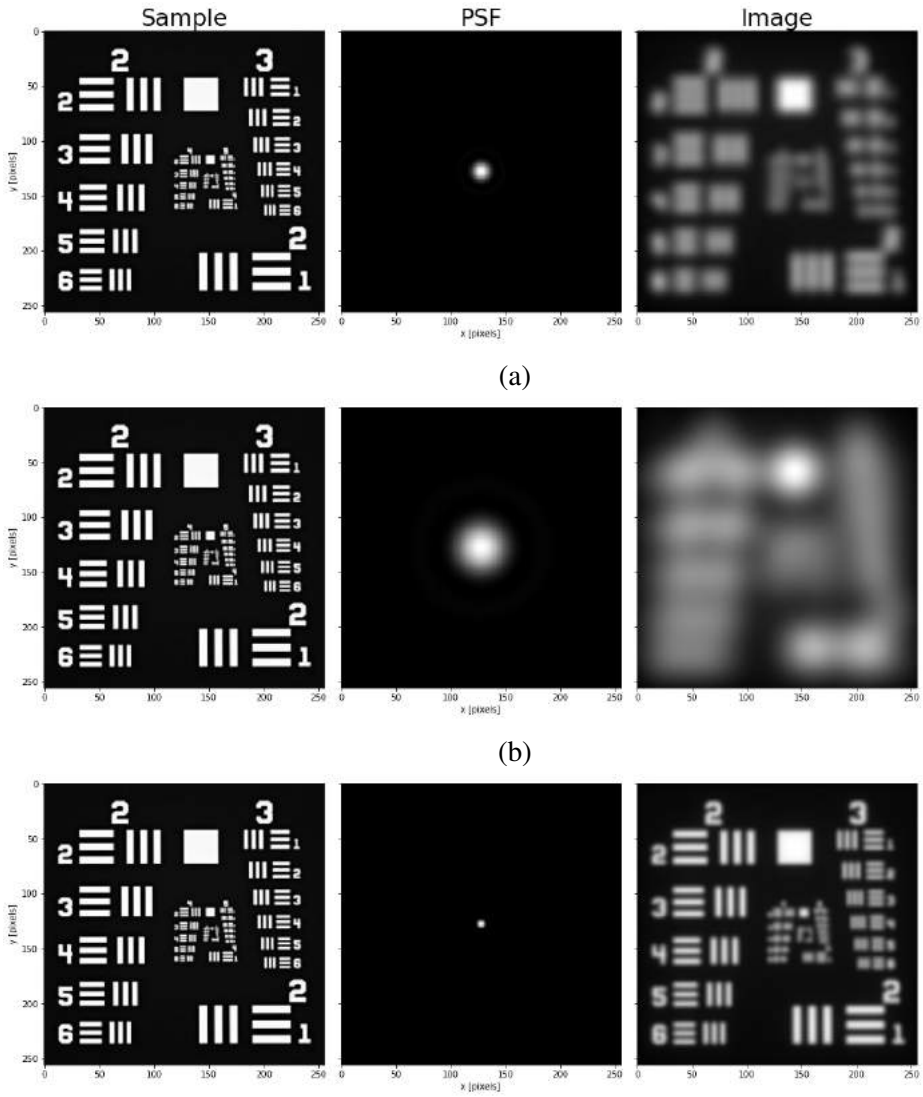

Figure 3: *The effect of the PSF visualized. The sample (left column), a USAF Test chart (256 by 256 pixels), is convolved with a PSF of arbitrary size (middle column). The resulting image is a blurred chart (right column). Furthermore, if the size of the PSF is increased, the image becomes even more blurry. A smaller PSF gives a sharper image. If a high-resolution image is to be obtained, the PSF must therefore be as small as possible.*

Diffraction and the Airy disk

When it comes to the limitations of an optical system, the most important one to discuss is *diffraction*. This phenomenon occurs when rays (electron or light) pass through an aperture to be focused on a sample. When assuming a perfect lens with a circular aperture, the best-focused spot obtainable in an optical system limited by diffraction is the *Airy disk* [12], named after George Biddel Airy (1801-1892). The Airy disk is a PSF characterized by a centered bright spot surrounded by concentric circles of decreasing intensity, see figure (4).
The radius r_{Airy} from the center of the bright spot in the center to the first zero (radius to first

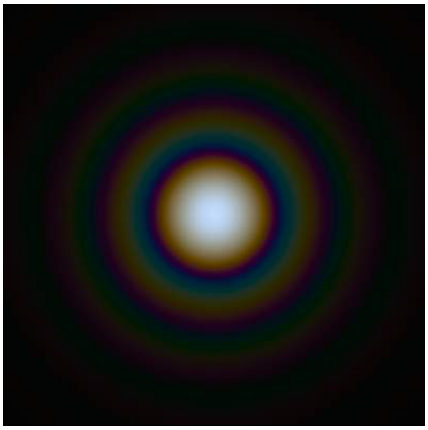

(a) *A computer-generated Airy disk from diffracted white light*[12].

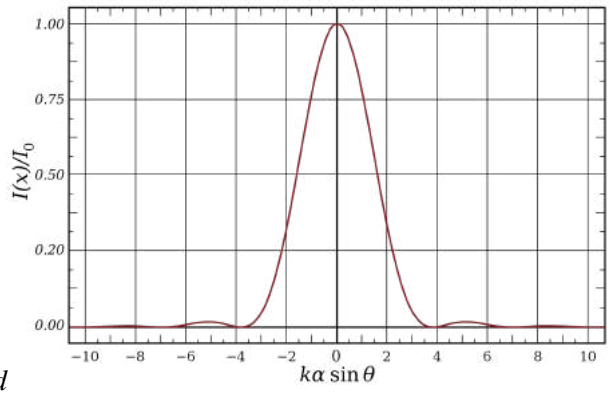

(b) *1D Airy pattern.*[12]

Figure 4: *Computer-generated Airy disk from diffracted white light (left) and a 1D representation of an Airy pattern (right).*

zero intensity) is $r_{Airy} \approx 20 - 40\text{nm}$ for a standard SEM measurement. Since the Airy disk is the diffraction-limited ideal probe shape, it is used as the just-focused PSF $g(x, y)$. A 2D Airy pattern is often approximated by a Gaussian function, see figure (5) [12]. The differences between an Airy pattern and a Gaussian function become more apparent when approaching the first zero at distance r_{Airy} from the center of the Airy pattern. As $r = \sqrt{x^2 + y^2} \to r_{Airy}$, the

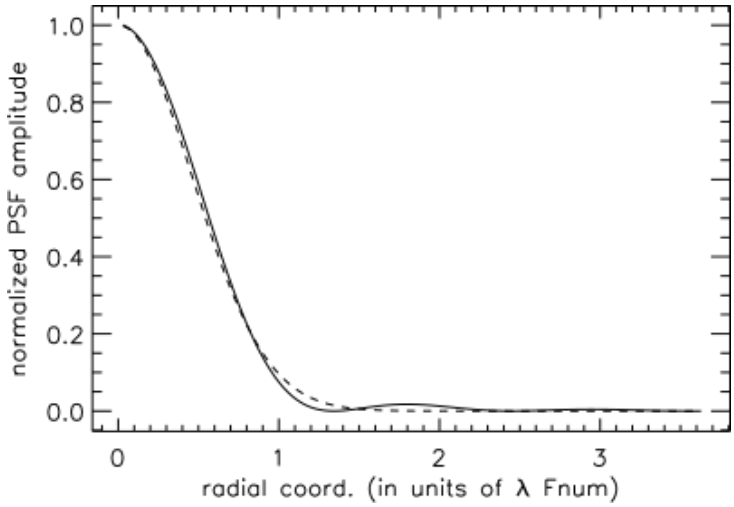

Figure 5: *Radial cross-section through an Airy pattern (solid line) and the Gaussian function used to approximate the Airy pattern (dashed). It is clear to see that for the intensity points larger than* 0.2*, the Airy pattern and Gaussian are very similar [12].*

Gaussian function differs from the Airy pattern. Up to intensity 0.2, the normalized Gaussian and Airy patterns are very similar. This Airy disk function $g(x, y)$ is therefore approximated by a normalized Gaussian function [12], with mean $\mu_{Airy} = 0$ and standard deviation σ_{Airy} related to the Airy radius r_{Airy} in the following way:

$$\sigma_{Airy} = \frac{0.84}{1.22} r_{Airy} \approx 0.689 r_{Airy}. \tag{7}$$

It follows that the Gaussian function $g(x, y)$ used as the just focused PSF is:

$$g(x, y) = \exp\left(-\frac{x^2 + y^2}{2\sigma_{Airy}^2}\right). \tag{8}$$

Point spread function in wavefront optics

So how is the shape of the PSF formed? For that, let us take to look at Wavefront optics. From quantum physics, it can be inferred that electrons are not only describable as particles but also as waves. The electrons passing through the objective lens can therefore be expressed as a spherical *wavefront* [13]. Ideally, this wavefront is diffracted and then converges to a single focal point on the image plane when passing through the objective lens. Due to limitations of the optical system, the phase of the diffracted wavefront shifts in various locations. This results in the wavefront landing on the image plane in a distorted, stretched shape, called the *aberrated wavefront*. This shape is defined as the complex Point Spread Function of the system. Given the ideal, diffracted wavefront $S(x, y)$, the aberrated wavefront $W(x, y)$ is described as follows:

$$W(x, y) = S(x, y) \exp\left(-i\Phi(x', y')\right), \tag{9}$$

where $\Phi(x', y')$ is the aberrated phase, with (x', y') the gradient (or angle/orientation) of image plane coordinates (x, y). The optical system is illustrated in figure (6). Plane waves with wavelength $\lambda \sim 10^{-12}\,\mathrm{m}$, describing the electron beam in a typical SEM measurement, travel in the positive z-direction and enter a circular pupil plane with radius ρ_0, which represents the objective lens of the SEM (see figure (1b)), and Cartesian coordinates (u, v). The action of passing through the pupil deforms the plane wave into an aberrated wavefront W. The wavefront travels from the pupil plane and creates an intensity profile I on the image plane (x, y) at a distance from the pupil plane. Ideally, the distance between the pupil and image plane is the focal length f of the objective lens. It is for this reason we define the image plane to be located on $z = 0$, the pupil plane is therefore located on $z = -f$. The focal length f and aperture radius ρ_0 define the Numerical Aperture NA of the system:

$$NA \equiv \frac{\rho_0}{f}, \tag{10}$$

where the Numerical Aperture is assumed small, $NA \leq 20\,\mathrm{mrad}$.

The intensity profile I can be equated to the absolute value of the complex PSF $g(x, y)$. Furthermore, this complex intensity profile $g(x, y)$ is also described by the diffraction integral [14] in Cartesian coordinates:

$$g(x, y) = \int_{-\infty}^{\infty}\int_{-\infty}^{\infty} W(X, Y) \exp\left(-i\frac{2\pi}{\lambda}(Xx + Yy)\right) \mathrm{d}X\,\mathrm{d}Y, \tag{11}$$

where W is defined in equation (9). The aberrated phase function $\Phi(x, y)$ is an infinite polynomial series with coefficients C_n^m that serve as weights for each polynomial of power m of the series [1]. These coefficients are defined as *aberration coefficients*. By simulating Φ for a small set of aberrations, the method used for aberration retrieval can be tested.

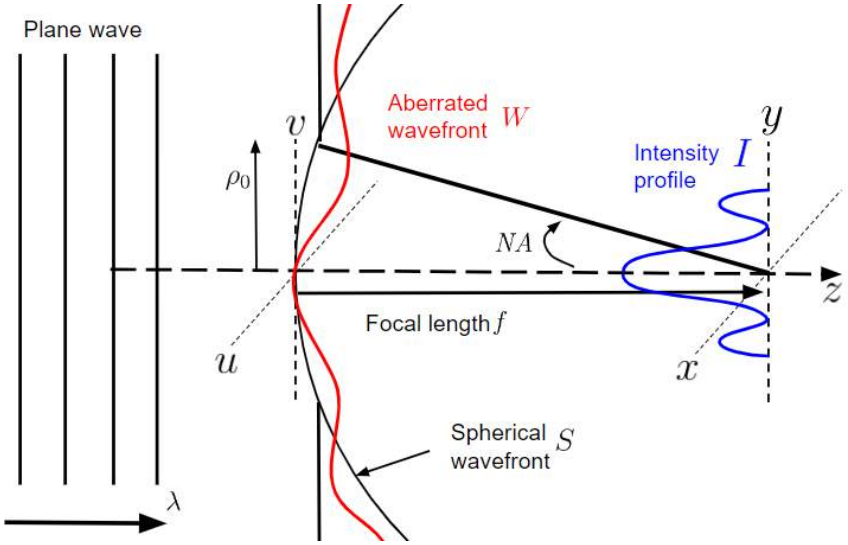

Figure 6: *Geometry of the optical system described by wavefront optics. From the left, plane waves with wavelength λ enter a circular pupil. The action of passing through the pupil distorts the plane wave into an aberrated wavefront W. An ideal spherical wavefront S is also depicted as a reference. The aberrated wavefront travels further in the positive z-direction until it lands on the image plane denoted by coordinates (x, y), and forms an intensity profile I, which is the measurable quantity in an SEM. This intensity profile is equal to the absolute value of the complex PSF $g(x, y)$ defined in equation (6). The image plane is ideally placed at focal length f from the pupil with radius ρ_0. These quantities define the Numerical Aperture of the pupil $NA \equiv \rho_o / f$.*

Aberrations

There are other limiting factors of an optical system aside from diffraction. Imperfections in the alignment or design of various components in the SEM, as well as the electron beam voltage, influence the shape of the spot with which the electron beam hits the sample. The resulting deviations in the spot shape of an optical system due to these imperfections are called *aberrations*. In this report, we focus on a subset of geometrical aberrations up to the second order and include third-order spherical aberration. [13]. In wavefront optics, aberrations express themselves in the aberrated phase function Φ, see equation (9). This function Φ is a polynomial up to infinite order, with coefficients C_n determining the weight of each part of the polynomial. These coefficients are called *aberration coefficients*. By measuring an SEM image out of focus, various aberrations express themselves more clearly in their PSFs. Figure (7) [1] depicts how the shape of the probe changes with various aberrations: each shape depicts a different aberration and has its own coefficient. The just-focus probe shapes change very little compared to the out-of-focus probes. When calculating aberrations from SEM images, this probe shape is often approximated by a Gaussian function.

Figure (7) also shows how the probe shapes differ for under- and over-focus: aberrations are well-represented in the under- and over-focus probe shapes. The aberrations are arranged based on their order [1], denoted in their subscripts, except for defocus C_{df}, which is first-order, and third-order spherical aberration C_s. This report focuses on geometrical aberrations up to second order and includes third-order spherical aberrations. Without aberrations, the probe is the

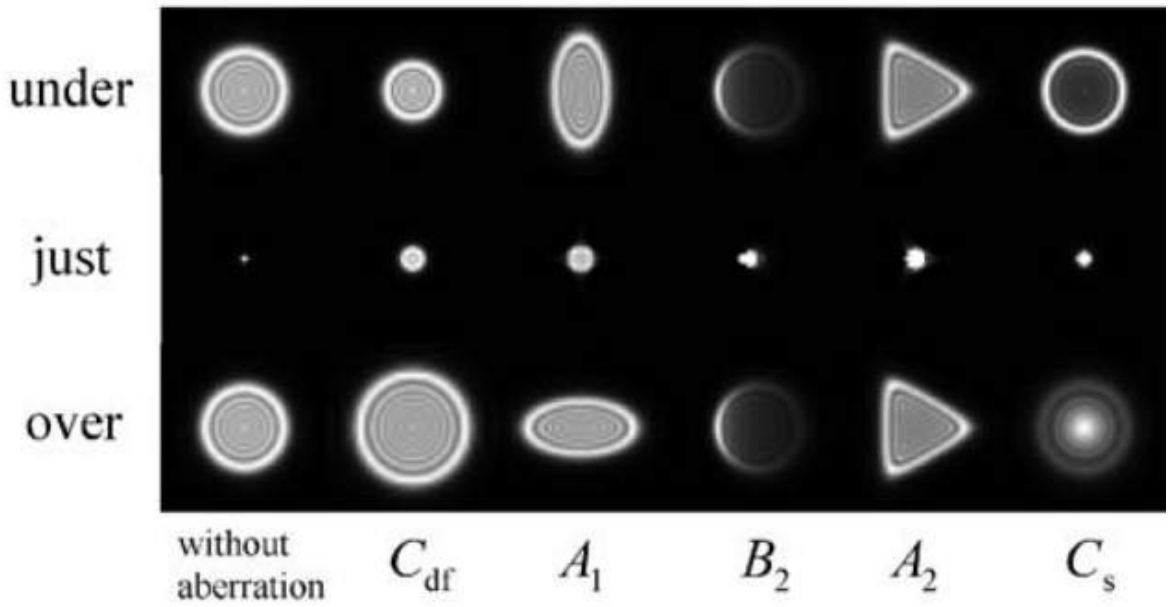

Figure 7: *Simulated probe shapes for under, just and over focus depicting aberrations up to second order. The orders of the aberrations are denoted in the subscripts of the coefficients, except for defocus C_{df}, which is first-order, and third-order spherical aberration C_s [1].*

same size and shape under- and over-focus. The first-order aberrations are defocus $C_{df} \in \mathbb{R}$ and first-order astigmatism $A_1 \in \mathbb{C}$. C_{df} is characterized by the difference in size between the probes and A_1 by the longitudinal and transversal stretching when under- and over-focus. The second-order aberration coma $B_2 \in \mathbb{C}$ can be identified by the intensity trails on one side, and astigmatism (second-order) $A_2 \in \mathbb{C}$ by the three-fold symmetry in the probe shape. Furthermore, the probe shapes are the same between under- and over-focus. Finally, spherical aberration $C_s \in \mathbb{R}$ is distinguishable by the intensity distribution differences between the under- and over-focus probes. Important to note is the fact that A_1, A_2, and B_2 are complex. The aberrations that these coefficients represent are not radially symmetrical, as can be seen in figure (7). The argument of these aberration coefficients determines the orientation of the probe shape.

For these five aberrations, the aberrated phase $\Phi(x', y')$ is defined for complex gradient coordinate $u' = x' + iy'$ [1]:

$$\Phi(u') = \frac{2\pi}{\lambda} \mathrm{Re}\left\{ \frac{1}{2} C_{df} |u'|^2 + \frac{1}{2} A_1 \bar{u'}^2 + \bar{B_2} |u'|^2 \bar{u'} + \frac{1}{3} A_2 \bar{u'}^3 + \frac{1}{4} C_s |u'|^4 \right\}, \qquad (12)$$

where $\bar{u'}$ denotes the complex conjugate of u'. With this equation and the diffraction integral, it is possible to check if aberration retrieval methods are consistent for these five geometrical aberrations.

Defocus

Defocus $C_{df} \in \mathbb{R}$ [13] occurs when the sample is not located at the focal distance from the objective lens. The coefficient C_{df} is a measure of the distance between the actual focal distance

and the location of the sample.

Two-fold astigmatism

Two-fold astigmatism $A_1 \in \mathbb{C}$ [13] is caused by a difference in the horizontal and vertical focusing power of the objective lens. The lens is assumed to be a perfect circle. Of course, this can never be the case. Astigmatism causes the stretching of the under- and over-focus PSFs $g_{u,o}$. $A_1 \in \mathbb{C}$, indicating that the stretching can be oriented in any rotational direction, related to the argument of A_1, $arg(A_1)$. If $A_1 \in \mathbb{R}$, it means that the focusing power of the objective lens differs in the cardinal directions (x, y).

Second-order Coma

Coma $B_2 \in \mathbb{C}$ [13] occurs when electron rays enter the objective lens when not parallel to the optical axis. This causes the electron rays to diverge outward as the angle with which the rays enter the objective lens results in a comet-like shape in the image plane. In the PSFs $g_{u,o}$, this results in a skewed intensity distribution. The effect of B_2 does not differ between under- and over-focus.

Three-fold astigmatism

Three-fold astigmatism $A_2 \in \mathbb{C}$ is similar to two-fold astigmatism A_1 in that the focusing power of rays entering the objective lens differs depending on where the rays enter the lens. As the name suggests however, three-fold astigmatism exhibits three-fold symmetry in the PSFs $|g_{u,o}|$, and unlike A_1, the effect of A_2 does not differ between under- and over-focus.

Third-order spherical aberration

Spherical aberration $C_s \in \mathbb{R}$ [13] is caused by a difference in radial focusing power of the rays entering the objective lens. As rays enter the objective lens further away from the optical axis, their focusing power is altered based on the differing focusing power of the lens. If C_s is positive, this causes the intensity distribution to be *bimodal* under focus, and *unimodal* over focus [15]. Third-order spherical aberration is the most important aberration discussed in this report, as the SEM of the ImPhys department has a spherical aberration corrector, and it is the most prominent aberration in SEM measurements.

Probe shape line profiles

To compute the aberration coefficients for a set of under- and over-focus probes, we take N line profiles of the probes, with angle $\theta_k = \frac{k\pi}{N}$, with $k = 0, \cdots, N-1$ through the center of the probe. Imagine it like cutting a cake through its diameter N times, with the PSF representing the cake. From these line profiles, we calculate three characteristics [1]: asymmetry μ, width

σ, and curvature ρ using all points on the profile p_j, defined below:

$$\begin{aligned}\mu &= \frac{1}{W}\sum_j jp_j, \\ \sigma &= \sqrt{\frac{1}{W}\sum_j (j-\mu)^2 p_j}, \\ \rho &= \frac{\sigma^2}{T}\sum_{j\neq 0}\frac{1}{|j|}(p_j - p_0)p_j,\end{aligned} \tag{13}$$

with $j = 0, \pm 1, \pm 2, \cdots$ denoting the position on the line profile, $j = 0$ the center of the probe, and $W = \sum_j p_j$, $T = \sum_j p_j^2$. Note that the definition of σ is slightly different than in the source [1], which most likely used the assumption that $\mu = 0$ for calculating σ.

Characteristics

The characteristics μ and σ are defined as equivalent to the mean and standard deviation of a probability mass function respectively. The mean μ is used to represent the asymmetry of the line profile: if $\mu \neq 0$, then the line is not symmetric around the center of the line. Similarly the standard deviation σ can be used to represent the width of the line profile: an increase in σ indicates a higher variance of the line profile, and therefore the width of the line profile increases.
For curvature ρ there is no direct statistical equivalent. The expression for ρ seems to indicate the measure of a weighted difference between the intensity of the centroid p_0 and p_j. This is illustrated more clearly in figure (8) [1]. From the left, an electron beam with trajectories for spherical aberration crosses the image plane in the center of the image. In front of the image plane (under focus), the probe profile has a different shape than the probe profile behind the image plane (over focus). The mean μ and standard deviation σ stay the same for under- and over-focus. Furthermore, the center of the profile p_0 differs for under- and over-focus. The definition of curvature ρ describes a weighted distance between a point p_0 and p_j. The difference in curvature between under and overfocus is therefore a good measure for the effect of third-order spherical aberration C_s.

Aberration coefficients

The aberration coefficients are computed from the characteristics for each line profile of angle θ_k [1], described in Table 1, together with their typical order of magnitude O and symmetry. Note the dependence on $\exp(i\alpha\theta_k)$, with α denoting the symmetry of the aberration. For rotationally symmetric aberrations defocus C_{df} and spherical aberration C_s, $\alpha = 0$.

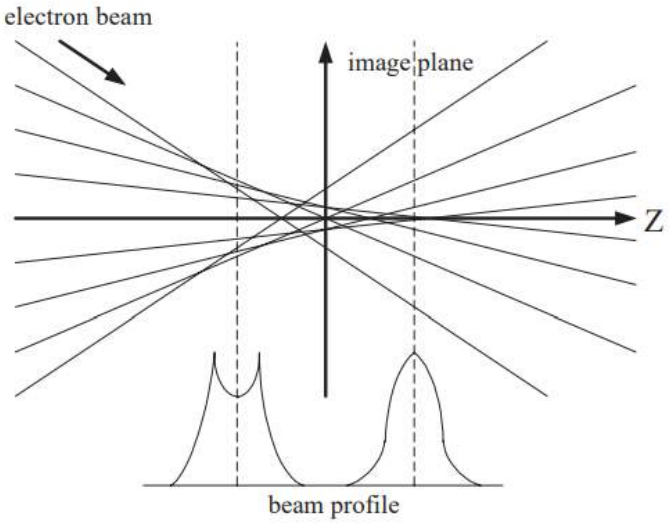

Figure 8: *From the left, an electron beam with trajectories for spherical aberration crosses the image plane in the center of the image. In front of the image plane (under focus), the probe profile has a different shape than the probe profile behind the image plane (over focus). The mean μ and standard deviation σ stay the same for under- and over-focus. Furthermore, the center of the profile p_0 differs for under- and over-focus. The definition of curvature ρ describes a weighted distance between a point p_0 and p_j. The difference in curvature between under and overfocus therefore represents the effect of spherical aberration best. [1].*

Table 1: *Aberrations with their order of magnitude O, symmetry and digitization. Note the dependence on $\exp i\alpha\theta_k$, with α denoting the symmetry of the aberration. For rotationally symmetric aberrations defocus C_{df} and spherical aberration C_s, $\alpha = 0$.*

Aberration	O **(in** m**)**	**Symmetry**	**Coefficient**	**Digitization**
Defocus	10^{-8}	Rotational	C_{df}	$\frac{1}{N}\sum_{k=1}^{N}(\sigma_{u,k} - \sigma_{o,k})$
Astigmatism	10^{-8}	Two-fold	A_1	$\frac{2}{N}\sum_{k=1}^{N}(\sigma_{u,k} - \sigma_{o,k})\exp(i2\theta_k)$
Coma	10^{-7}	One-fold	B_2	$\frac{2}{N}\sum_{k=1}^{N}(\mu_{u,k} + \mu_{o,k})\exp(i\theta_k)$
Astigmatism	10^{-6}	Three-fold	A_2	$\frac{2}{N}\sum_{k=1}^{N}(\mu_{u,k} + \mu_{o,k})\exp(i3\theta_k)$
Spherical aberration	10^{-3}	Rotational	C_s	$\frac{1}{N}\sum_{k=1}^{N}(\rho_{u,k} - \rho_{o,k})$

Methods

Introduction

This section presents an overview of the methods used to determine aberration coefficients from a series of images h_u, h and h_o. First, the complex-valued under- and over-focus PSFs g_u and g_o are obtained. After normalizing and cropping these PSFs, contours are traced around their shapes, and their centroids are calculated. Next, we trace N line profiles through the center of the probe, and for each line profile the characteristics described in equation (13) are computed. We then calculate the aberration coefficients as described in Table 1. Lastly, the benchmark used for this method of aberration retrieval is described.

Through-focus series

Figure (9) depicts a through-focus series of three images that will serve as an example. A just-focused image h is depicted on the left, under-focus h_u in the middle, and the over-focus image h_o on the right. The images depict an SEM measurement of a gold on carbon test specimen [16], particle sizes have a range of $5 - 150\text{nm}$. The field of view is $V = 2.6\ \mu\text{m}$ and the image is 3072×2188 pixels in size.

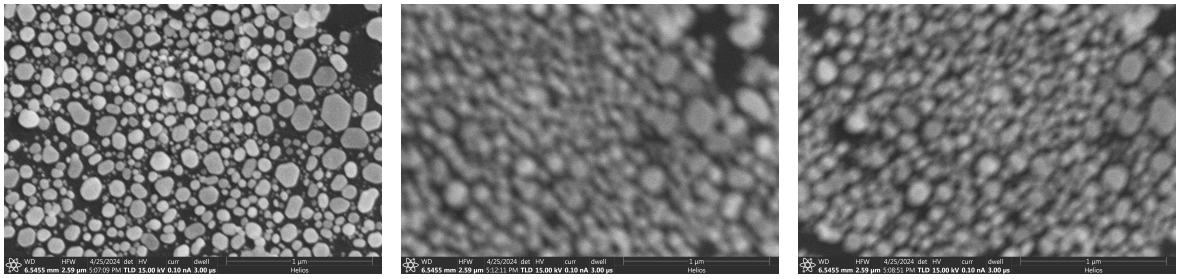

(a) *Just-focus image* h (b) *Under-focus image* h_u (c) *Over-focus image* h_o

Figure 9: *Through-focus series of images depicting an SEM measurement of a gold on carbon test specimen [16], with particle sizes* $5 - 150$ nm. *The field of view is* $V = 2.6\ \mu\text{m}$ *and the image is* 3072×2188 *pixels in size.*

Hanning window

Before the PSFs can be extracted from this through-focus series, the images are first windowed using a window function [17]. The 2D Fourier Transform is applied to the through-focus series of images by using the 2D Fast Fourier Transform (FFT) algorithm. The transformed images H and $H_{u,o}$ are subject to errors from leakage as a result [18]. To correct this problem, a window function is applied to the images before the FFT, in our case we use a *Hanning window*. The windowed images are shown in figure (10).

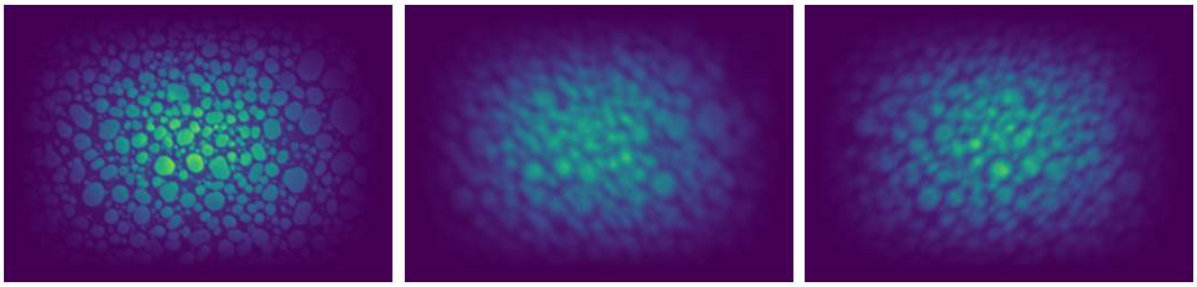

Figure 10: *Through-focus series of images from figure (9), windowed using a Hanning window [17]. Because the 2D FFT algorithm is used in the process of PSF extraction, a Hanning window function is applied to the images* h *and* $h_{u,o}$ *before the FFT.*

Pixel size

Pixel size is necessary to quantify when extracting Point Spread Functions from a through-focus series. The coefficients are defined in m, but the images are divided into pixels. Calculating the size of each pixel P_{size} is done easily when using a through-focus series:

$$P_{size} = \frac{V}{I_{max}}, \tag{14}$$

where V is the field of view depicted in the image, and I_{max} is the maximum amount of pixels on one axis. This quantity is vital for approximating the just focus PSF g, as the Gaussian function is generated in pixels instead of m, so $\sigma_{Airy} = 0.689\frac{r_{Airy}}{P_{size}}\ \mathrm{pixels}$. When generating the PSFs for the analysis of the PSF extraction method, the pixel size of the generated PSF needs to match the pixel size of the image. Typically, $P_{size} \sim 10^{-10}\ \mathrm{m}$, and in the case of the gold on carbon test sample shown in figure (9a), $P_{size} \approx 0.846\ \mathrm{nm}$.

Point spread function extraction

From equations (5) and (6) the complex point spread functions g_u and g_o are obtained and normalized. These PSFs are shown as their absolute values in figure (11), cropped around the center of the probe to more clearly see the difference, alongside the ideal, just-focused probe g. This just-focused probe is approximated with a 2D Airy pattern approximated by a Gaussian with mean $\mu = 0$ and standard deviation as defined in equation (7), radius $r_{Airy} \approx 20\times10^{-9}\mathrm{nm}$. The cropped PSFs $|g_u|$ and $|g_o|$ are used to determine the aberration coefficients defined in Table 1.

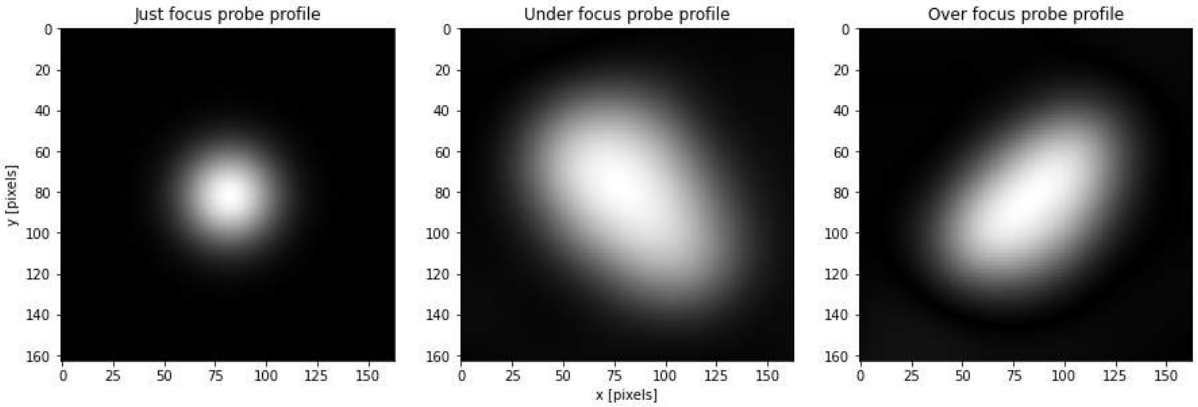

Figure 11: *Probe profiles extracted from the images in figure (9) From left to right: just-focused g, under-focused $|g_u|$ and over-focused $|g_o|$.*

Contours and centroids

After cropping the normalized PSFs $|g_{u,o}| \in [0, 1]$, a contour is traced around the shape of the PSFs in Python [19], where a function traces a contour around the normalized probe at a certain intensity level, $p_j = 0.2$ is used as boundary value. We denote the contour sets $C_{u,o}$, containing all points $|g_{u,o}|$ on and inside the contour. In other words, the contour $C_{u,o}$ is traced around all points (x, y) of $|g_{u,o}|$ that have intensity value $|g_{u,o}(x, y)| \geq 0.2$. This is shown in figure (12) with the blue contours around the PSFs. Furthermore, the centroids are also calculated from the contours by taking the coordinate mean of all points (x, y) in the contour, these are depicted as the red dots in the figure (12). The coordinates of these centroids are denoted $(x_{u,0}, y_{u,0})$ and $(x_{o,0}, y_{o,0})$ for under- and over-focus respectively.

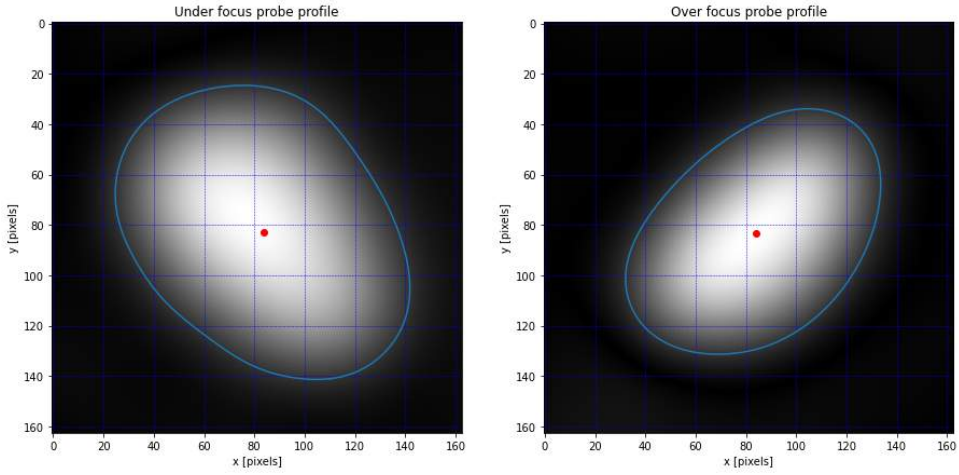

Figure 12: *under- and over-focus PSFs, $|g_u|$ and $|g_o|$ (left and right respectively) with contours $C_{u,o}$ (blue) traced around them and centroids $(x_{u,0}, y_{u,0})$ and $(x_{o,0}, y_{o,0})$ (red) plotted in the middle of the contour.*

Line profiles

The contours will serve as boundaries when determining the line profiles through the centroid of the probes. We take N line profiles through the centroids of the probes, these line profiles have angles $\theta_k = \frac{k\pi}{N}$, $k = 0, \cdots, N-1$. In this example, $N = 80$. First, the maximum distance d_u from the centroid to the edge of the image is calculated. Let w and l denote the width and length (in pixels) of the cropped PSF image. Then, the maximum distance from the centroid to the edge of the cropped image is:

$$d = \max(w - x_0, l - y_0). \tag{15}$$

The number of points M is chosen as the minimum of the width and length of the cropped images, omitting 4 pixels at the edge:

$$M = \min(w, l) - 4, \tag{16}$$

in the case of our example $M = 159$. We trace the line profiles as follows for each angle θ_k:

1. The direction vector $\vec{v_k}$ of the line profile is determined:

$$\vec{v_k} = \begin{pmatrix} \cos\theta_k \\ \sin\theta_k \end{pmatrix} \tag{17}$$

2. From the centroid $(x_{u,0}, y_{u,0})$, which has intensity value p_0 for $j = 0$, the coordinates of the points p_j on the profile line are computed for each j as follows:

$$(x_j, y_j) = (x_0 + j\frac{d}{\lfloor M/2 \rfloor}\cos\theta_k, y_0 + j\frac{d}{\lfloor M/2 \rfloor}\sin\theta_k), \tag{18}$$

   where $\lfloor M/2 \rfloor$ denotes the floor of $M/2$, i.e. $M/2$ rounded down to the nearest integer.

3. The coordinates (x_j, y_j) are rounded to the nearest integer, and from these coordinates the intensity values p_j are found in the PSF, but only if the coordinate is inside the contour $C_{u,o}$. If not, its intensity is set to $p_j = 0$.

The result is N line profiles through the centroid of the probe, each line profile with an angle θ_k and M intensity points p_j. This is illustrated in figure (13) for $N = 80$, $M = 159$. The lines individually are not straight, because the coordinates (x_j, y_j) are rounded to the nearest integer to select a specific pixel with intensity value p_j. Figure (14) depicts 4 line profiles for $k = 0, 20, 40, 60$ for under (left column) and over focus (right column) to illustrate this process. On the top row, the PSFs with contours and centroids are shown, with 4 profile lines drawn through the PSFs, centered on the centroid. On the second row the same profile lines are plotted as an intensity function of $j = \pm 1, \pm 2, \cdots, \pm\lfloor M/2 \rfloor$. The points outside the contour are automatically set to $p_j = 0$.

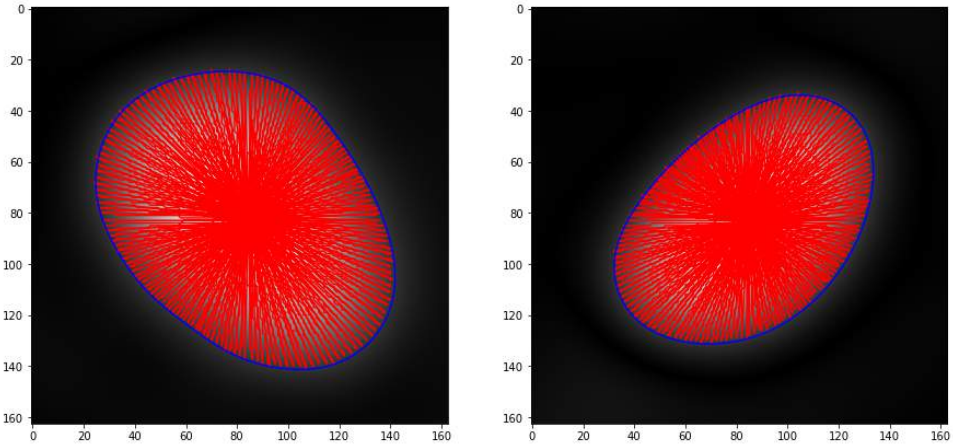

Figure 13: *under- and over-focus PSFs,* $|g_u|$ *and* $|g_o|$*, with* $N = 80$ *line profiles on their centroids. The lines are not straight because the coordinates* (x_j, y_j) *are rounded to the nearest integer to select a specific pixel with intensity value* p_j*.*

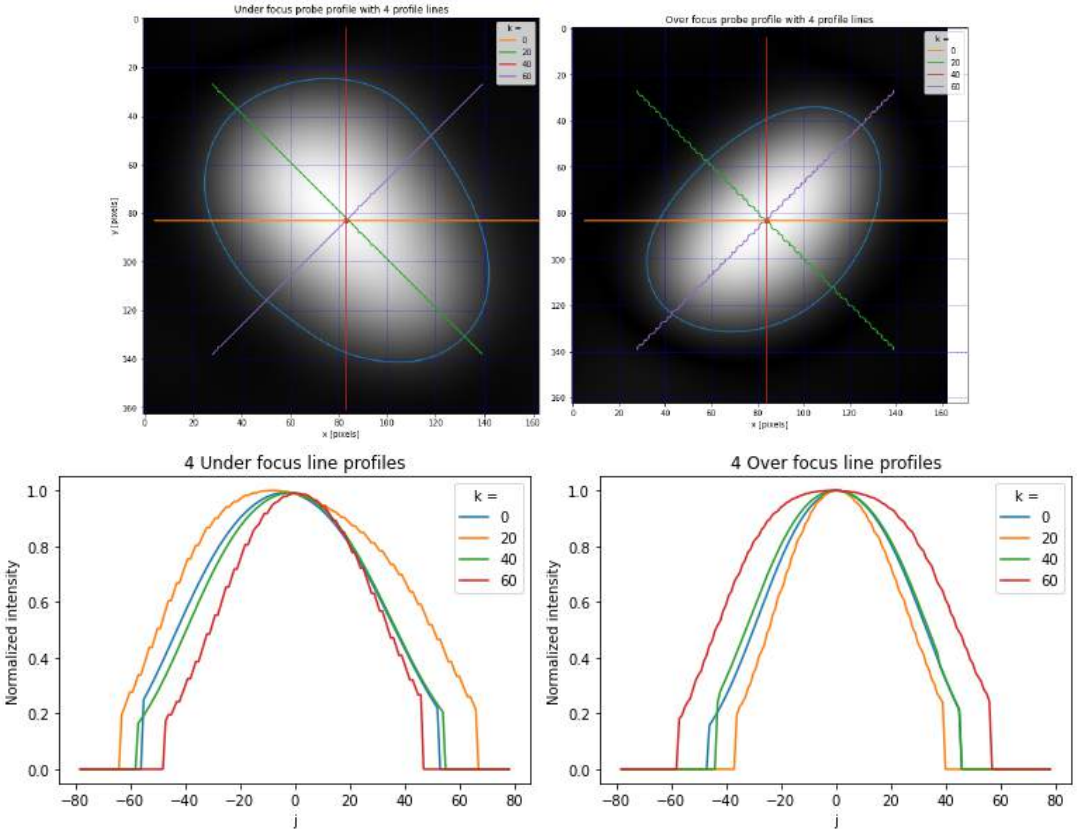

Figure 14: 4 *line profiles for* $k = 0, 20, 40, 60$*. Above the probe shapes with contours and centroids are plotted alongside the profile lines. Below the normalized intensity of these same profile lines are plotted as a function of* $j = \pm 1, \pm 2, \cdots, \pm\lfloor M/2 \rfloor$*. The points outside the contour are automatically set to* $p_j = 0$*.*

Characteristics

For each line profile with angle θ_k, three characteristics are calculated using equation (13): width σ, asymmetry μ and curvature ρ.

The first two characteristics asymmetry μ and width σ are expressions for the discrete mean and discrete standard deviation of a spatial probability distribution.

Aberration coefficients

Each aberration is defined as an average difference of characteristics between the under- and over-focus probes, see Table 1. For example, defocus with coefficient C_{df} is defined as the average difference in width σ between under- and over-focus:

$$C_{df} = \frac{1}{N}\sum_{k=1}^{N}(\sigma_{u,k} - \sigma_{o,k}). \tag{19}$$

The characteristics whose difference defines these aberration coefficients are chosen based on how the PSFs change with these aberrations.

For all complex coefficients, which represent aberrations with two degrees of freedom (i.e. A_1, B_2 and A_2), the average difference for each θ_k is multiplied with a complex exponent $2\exp(i\alpha\theta_k)$, with α representing the symmetry of the aberration, and 2 representing the degrees of freedom (see Table 1). The calculated aberration coefficients are depicted in Table 2. It is assumed that the digitizations have the order of magnitude as defined in Table 1. Additionally, figure (15) depicts the moduli of the extracted aberration coefficients in a horizontal bar plot. We can see that two-fold astigmatism has the largest contribution. This concludes the process of aberration coefficient retrieval.

Table 2: *Aberration coefficients and their calculated values extracted from the spot shapes in figure (12) based on the equations listed in Table 1.*

Aberration coefficient	**Retrieved value**	O **(in** m**)**
C_{df}	4.325	10^{-8}
A_1	$0.07360 + i9.284$	10^{-8}
B_2	$-0.6404 + i0.082615$	10^{-7}
A_2	$-1.241 + i1.469$	10^{-6}
C_s	-1.081	10^{-3}

Coefficient extraction test

By generating PSFs using the diffraction integral, see equation (11), the method of calculating aberration coefficients is tested. The extracted coefficients are then plotted in bar plots, to check if the generated aberrations in the PSF are successfully extracted when compared to other extracted aberrations. For example, if we add only $C_{df} = 0.5\ \mu\mathrm{m}$, we simulate the effects shown in figure (7) in a through-focus series. We do this for the five aberrations depicted in figure (7).

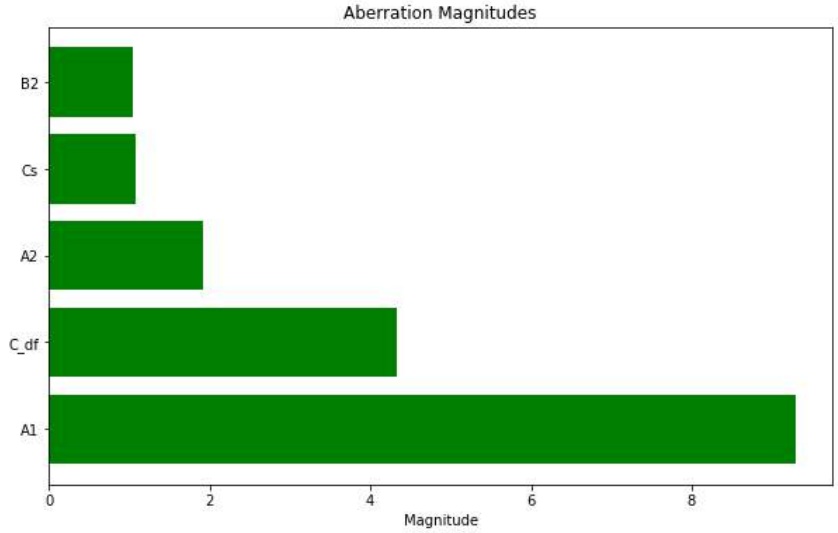

Figure 15: *Bar plot depicting the moduli $|C_n|$ of the extracted coefficients. We can see that two-fold astigmatism $|A_1|$ has the largest value.*

Benchmarking

To test this method of aberration retrieval, PSFs with known aberration coefficients are simulated using the diffraction integral, see equation (11). Afterward, the aberrations are retrieved using the methods described in this chapter, starting from drawing contours and calculating the centroids. To this end, we define $Q(C_n)$ as the ratio between the pre-determined aberration coefficients C'_n and the retrieved aberration coefficients C_n:

$$Q(C_n) = \frac{C_n}{C'_n} \tag{20}$$

For each aberration coefficient in Table 1, we start from an arbitrary value $C'_{n,1}$, and calculate $Q(C_n, s)$ using the methods described in this chapter. The other aberration coefficients are set to zero. We repeat this process for multiple factors $sC'_{n,1} = C'_{n,s}$: with $s \in [1, S]$, $S \in \mathbb{N}$. If the aberration retrieval method is accurate, the retrieved coefficients $C_{n,s}$ should scale equally to $C'_{n,s}$ with this factor. In other words, $Q(C_n, s)$ should stay constant when plotted against s:

$$Q(C_n, s) = \frac{C_{n,s}}{sC'_{n,1}} \tag{21}$$

As an example, we generate an artificial PSF using a code that applies equation (11) to generate under- and over-focus PSFs with predetermined aberration coefficients. Initially, we add a small amount of spherical aberration $C'_{s,1} = 60\mu\text{m}$, with the second subscript 1 denoting $s \in [1, S]$. We repeatedly generate PSFs with increasing amounts of $C'_{s,s} = sC'_{s,1}$. Let $S = 50$, as such we generate 50 PSFs, only containing increasing amounts of C_s. Five of these PSFs are shown in figure (16), for $s = 10, 20, 30, 40, 50$. For each PSF, we use the methods described in this chapter to retrieve the aberration coefficient C_s, and then calculate $Q(C_n, s)$ as defined above for each retrieved coefficient. The other samples for $S = 50$ are shown in the appendix.

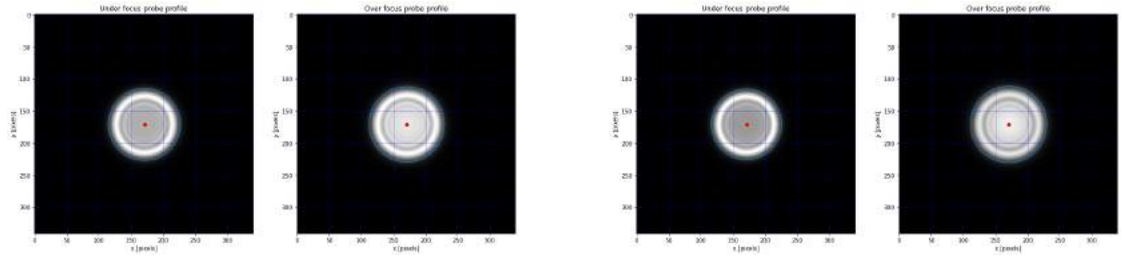

(a) $s = 10$

(b) $s = 20$

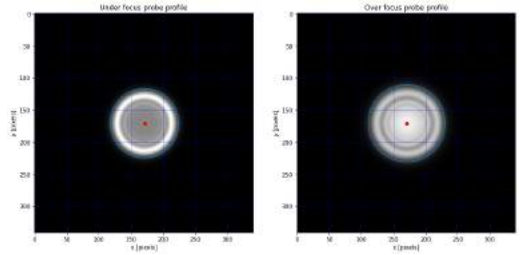

(c) $s = 30$

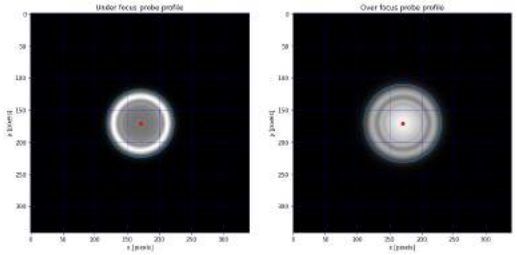

(d) $s = 40$

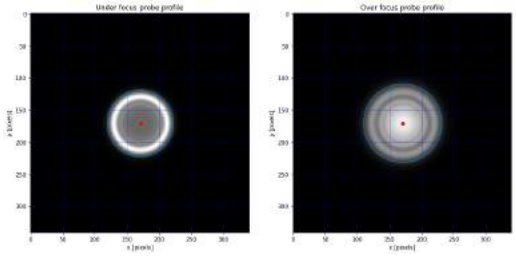

(e) $s = 50$

Figure 16: *Simulated PSFs imitating spherical aberration with coefficients* $C'_{s,s} = sC_{s,1}$, $C'_{s,1} = 60\ \mu\text{m}$, *see Table 4. The PSFs are shown for* $s = 10, 20, 30, 40, 50$. Additionally, their contours and centroids are plotted, as a check if my code successfully retrieved the spot shape.

Results

Introduction

This chapter presents the results of the experiments testing the aberration retrieval method. To this end, we simulate various under- and over-focus PSFs imitating the shapes as presented in figure (7). From there, we test the PSF extraction method by convolving the simulated PSF with the gold on carbon test image in figure (9a), with a given field of view $V = 2.59\ \mu\mathrm{m}$, to simulate a through-focus series of images. Next, the PSFs $g_{u,o}$ are extracted from this virtual through-focus series. The aberration coefficient retrieval method described in the previous chapter is then applied to both the simulated PSFs $g'_{u,o}$ and extracted PSFs $g_{u,o}$. The moduli of the retrieved coefficients from analyzing both $g'_{u,o}$ and $g_{u,o}$ are shown in a bar plot. Finally, we compare the input coefficients used to simulate the PSFs $g'_{u,o}$ and the coefficients retrieved from $g_{u,o}$.
From these experiments, it is clear that the PSF extraction method is implemented successfully, as the extracted shapes and coefficients of the PSFs $g_{u,o}$ do seem to match those of the simulated PSFs $g'_{u,o}$. However, the input coefficients used for simulating $g'_{u,o}$ do not match the retrieved coefficients. There is a mismatch in magnitude for all coefficients and in the argument for the complex coefficients A_1, B_2, and A_2. Suggestions to match the arguments are made. Lastly, the results of the Benchmark test described in the section on Methods are given for all aberration coefficients. From these results, we infer that the coefficient retrieval method is consistent for defocus C_{df}, spherical aberration C_s, and two-fold astigmatism A_2.

Test images

The method of aberration retrieval described in the Methods chapter of this report is tested with the just-focus image depicted in figure (9a). After a Hanning window is applied, this test image is convolved with simulated PSFs g'_u and g'_o that simulate the shapes in figure (7) with added defocus coefficients $C_{df} = \pm 1\ \mu\mathrm{m}$. We do this individually for each of the five presented aberrations. An example is shown in figure (17). In (17a) the test image is shown on the left. Next to the test image, an under-focus and over-focus image are shown in the middle and on the right of (17). These images are created with simulated PSFs that simulate only spherical aberration $C'_s = 5\ \mathrm{mm}$. The simulated PSFs $|g'_{u,o}|$ that are convolved with h to simulate the through focus images $h_{u,o}$ are shown in figure (17b). The images $h_{u,o}$ generated from the test image, together with the simulated PSFs can be found in the appendix for the other four aberrations.

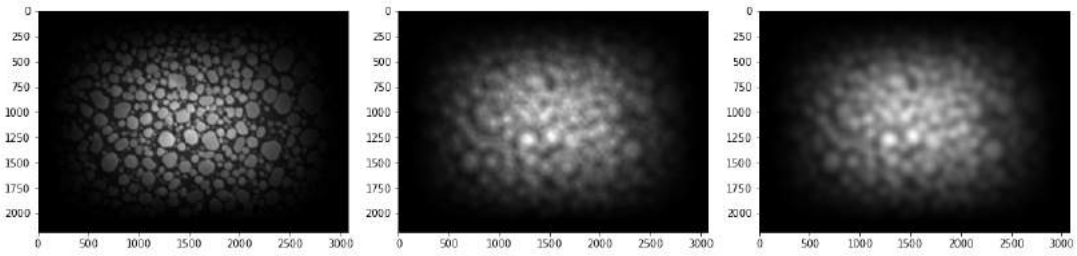

(a) *Simulated through-focus series.*

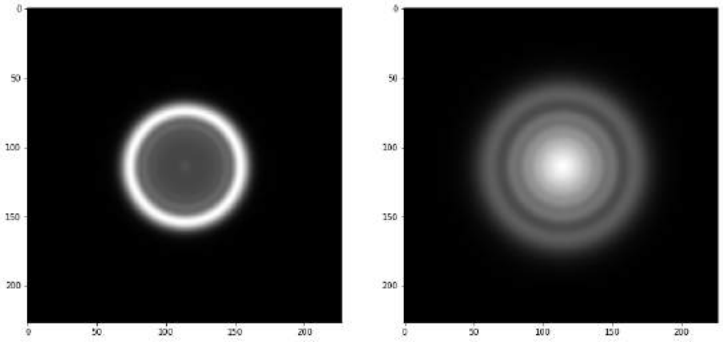

(b) *Simulated PSF depicting the effects of positive spherical aberration C_s. Under focus $|g'_u|$ on the left, over focus $|g'_o|$ on the right.*

Figure 17: *Gold on carbon test image [16] after the application of a Hanning window. In (17a) the tin-on-carbon test image is shown on the left. Next to the test image, under- and over-focus images are shown in the middle and on the right respectively. These images are created with simulated PSFs shown in (17b), that simulate only spherical aberration $C_s = 5$ mm.*

PSF extraction

To test the extraction method, we compare the simulated PSFs $|g'_{u,o}|$ to the extracted PSFs $|g_{u,o}|$. The images depicted in figure (17a) are used as our just-, under- and over-focus images h, h_u, and h_o respectively. For the reference just-focused probe g a Gaussian function as described in equation (8), with Airy radius assumed $r_{Airy} = 20$ nm. The rest of these probe shape comparisons can be found in the appendix. The extracted shapes match the shapes of the simulated PSFs used to generate the images. Results indicate that the PSF extraction method as described in equations (5) and (6) are implemented successfully, as the shapes of the retrieved PSFs in figure (18) do seem to match the shapes of the simulated PSFs in figure (17).

Aberration coefficient retrieval

Profile lines

Figure (19) depicts the same PSFs shown in figure (18), now with $N = 80$ profile lines traced through the centroid of the probes, contained in the contours. All profile line points $p_j \notin C_{u,o}$ are automatically set to $p_j = 0$. Below, an image depicting the profile lines for $k = 0, 20, 40, 80$ are shown.

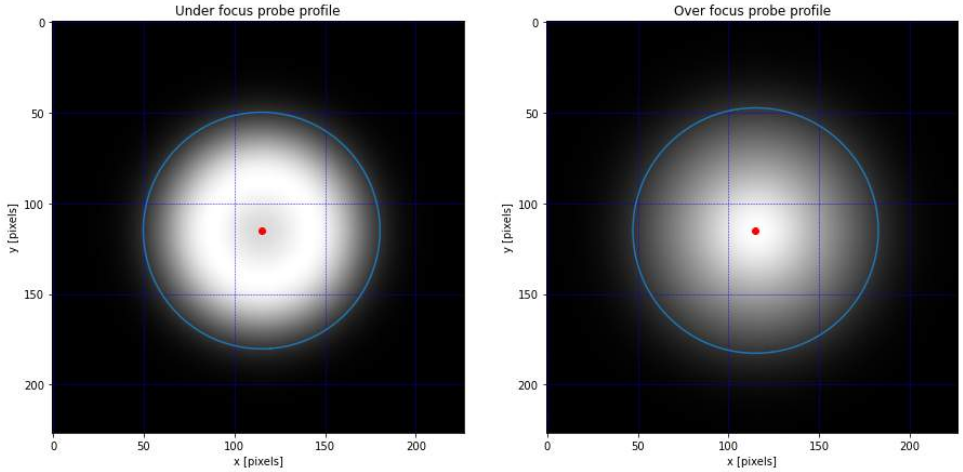

Figure 18: *Extracted under- and over-focus PSFs* $|g_{u,o}|$ *with their contours (blue) and centroids (red). The extracted shapes match the shapes of the simulated PSFs used to generate the images, see figure (17b).*

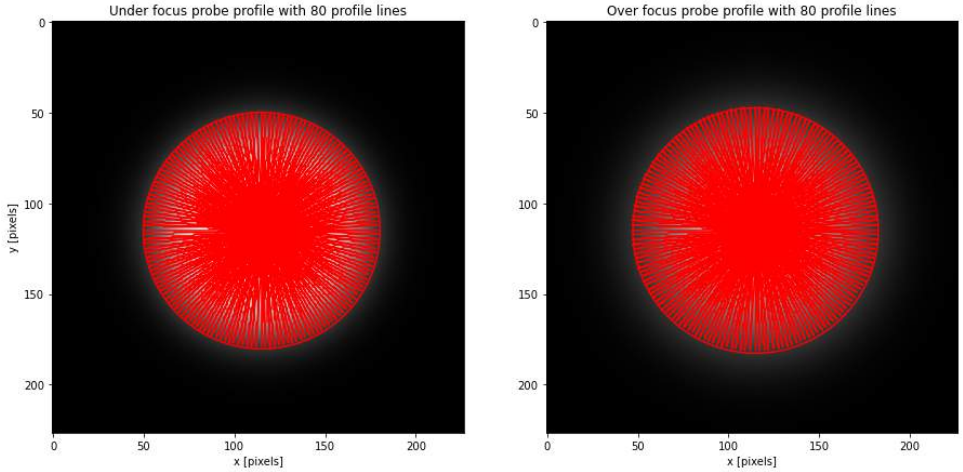

(a) $N = 80$ *profile lines.*

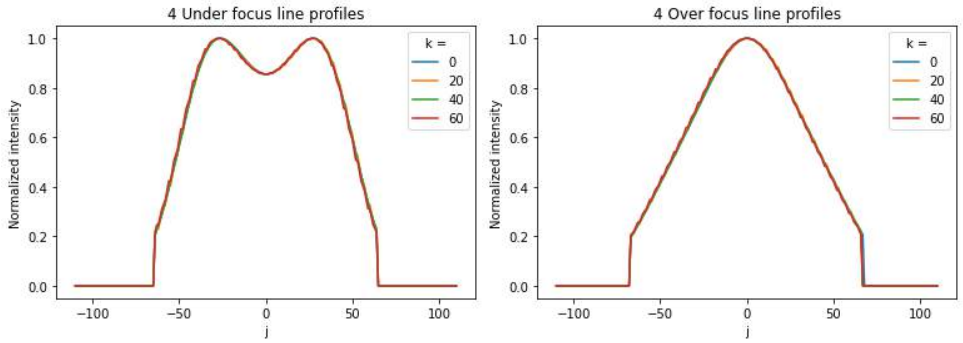

(b) *Under focus profile lines.* (c) *Over focus profile lines.*

Figure 19: *Probe profiles for* $|g_{u,o}|$ *with* $N = 80$ *profile lines drawn through their centroids, contained within the contours* $C_{u,o}$*. All profile line points* $p_j \notin C_{u,o}$ *are automatically set to* $p_j = 0$*. Below, a plot depicting profile lines for* $k = 0, 20, 40, 80$ *are shown.*

Aberration coefficients

Figure (20) shows the modulus or absolute value of the aberration coefficients retrieved in a bar plot. These coefficients are determined from the profile lines drawn and shown in figure (19a) using equations (13) and Table 1. The coefficients retrieved from the extracted PSFs $g_{u,o}$ in orange are compared to the coefficients retrieved by analyzing the original simulated PSFs $g'_{u,o}$ (see figure (17b)) in blue. From the bar plot, it is clear that spherical aberration C_s is the largest calculated aberration coefficient. There is a large difference in magnitude between the retrieved coefficient in blue (simulated) compared to the coefficient in orange (extracted). The resulting bar plots of the other simulated coefficients can be found in the Appendix. For defocus C_{df}, two-fold astigmatism A_1 and coma B_2, the retrieval method correctly selects the simulated coefficients as the ones with the highest magnitude. For three-fold astigmatism A_2, coma is selected as the coefficient with the highest magnitude, after A_2.

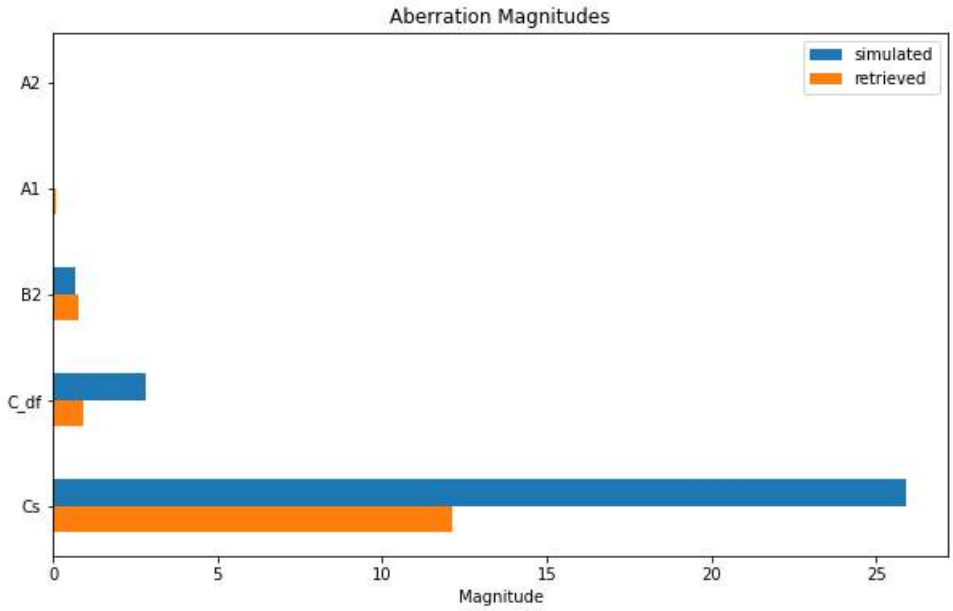

Figure 20: *Bar plot depicting the modulus of the aberration coefficient retrieved using the line profiles and equations in Table 1. Spherical aberration C_s is by far the largest coefficient. However, the magnitude does not match the input coefficient $C'_s = 5$ mm.*

Simulated vs retrieved coefficients

The retrieved aberration coefficients C_n from simulating shapes with singular aberration coefficients C'_n are shown in Table 3. There is a mismatch in magnitude and argument for most of the retrieved aberration coefficients. For defocus C_{df}, the retrieved coefficients are always negative compared to the input coefficients. Two-fold astigmatism A_1 correctly retrieves the highest magnitude of its real and imaginary parts $A_{1,r}$ and $A_{1,i}$, but does not correctly retrieve the argument of $A_{1,i}$. Second-order coma B_2 does not match in the slightest, not even in terms of argument. The retrieval method mixes up the magnitudes of the real and imaginary parts of B_2. Additionally when simulating three-fold astigmatism, due to the similarities in definition between B_2 and A_2, the method retrieves a larger amount of coma than three-fold astigmatism,

even though no coma was simulated in the PSFs. Three-fold astigmatism is also similar to coma, as the retrieval method also gives a larger magnitude to the imaginary part of A_2 when the simulated coefficient A_2' is real, and vice versa for imaginary A_2'. Finally, spherical aberration C_s does have the correct sign, and the method does retrieve C_s as the coefficient with the highest magnitude.
In conclusion, the aberration coefficient retrieval method does select the correct aberration coefficient for defocus C_{df}, spherical aberration C_s, two-fold astigmatism A_1 and coma B_2 to be the coefficient with the largest modulus magnitude, and not for three-fold astigmatism A_2. However, the arguments of A_1, B_2, and A_2 do not match the input arguments. Further recommendations and suggestions can be found in the next section on Discussion.

Table 3: *Simulated vs retrieved aberration coefficients. There is a mismatch in magnitude and argument for most of the retrieved aberration coefficients.*

Aberration coefficients	**Input simulation** (in μm)	**Retrieved value**
C_{df}	0.5	-29.56
	-0.5	29.562
$A_1 = A_{1,r} + iA_{1,i}$	$0.2 + i0$	$1.651 - i0.005930$
	$-0.2 + i0$	$-1.651 + i0.005930$
	$0 + i0.2$	$-0.006403 - i10.29$
	$0 - i0.2$	$0.006403 + i10.29$
$B_2 = B_{2,r} + iB_{2,i}$	$8 + i0$	$-1.147 - i7.765$
	$-8 + i0$	$2.422 + i8.699$
	$0 + i8$	$8.847 + i2.288$
	$0 - i8$	$-11.40 - i4.685$
$A_2 = A_{2,r} + iA_{2,i}$	$20 + i0$	$4.459 - i8.718$
	$-20 + i0$	$-4.660 + i9.188$
	$0 + i20$	$-9.163 + i4.614$
	$0 - i20$	$8.762 - i4.430$
C_s	5000	12148
	-5000	-12148

Benchmark results

The results of benchmarking the aberration retrieval method are shown in this section. As in the previous sections, the process is explained with spherical aberration C_s as an example. Images of other aberrated PSFs can be found in the appendix.

First, the initial aberration coefficients $C'_{n,1}$ are defined in Table 4. Next, under- and over-focus PSFs $|g_{u,o}|$ are generated for $s \in [1, S]$. These are shown in the Methods chapter for C_s, see figure (16), and in the appendix for C_{df}, A_1, B_2 and A_2. Finally, the (s, Q)-plots are shown for spherical aberration C_s in figure (21a), defocus C_{df} in figure (21b), two-fold astigmatism A_1 in figure (22), coma B_2 in figure (23) and three-fold astigmatism A_2 in figure (24). For the simulations, we took $N = 80$ and $S = 50$. It is assumed that the retrieved coefficients are of order magnitude as noted in Table 1.

From these (s, Q) plots it is clear that the retrieval of defocus C_{df}, spherical aberration C_s and three-fold astigmatism A_2 remains consistent with the increase in coefficient. For two-fold

astigmatism A_1 and coma B_2 this can not be said.

Table 4: *Initial aberration coefficients $C'_{n,1}$ for the simulations. The real and imaginary parts of the coefficients are used individually, and the other coefficients are set to* 0.

Aberration coefficient	**Value** (in μm)
$C'_{df,1}$	0.01
$A'_{1,r,1}$	0.01
$A'_{1,i,1}$	0.01
$B'_{2,r,1}$	0.2
$B'_{2,i,1}$	0.2
$A'_{2,r,1}$	1
$A'_{2,i,1}$	1
$C'_{s,1}$	60

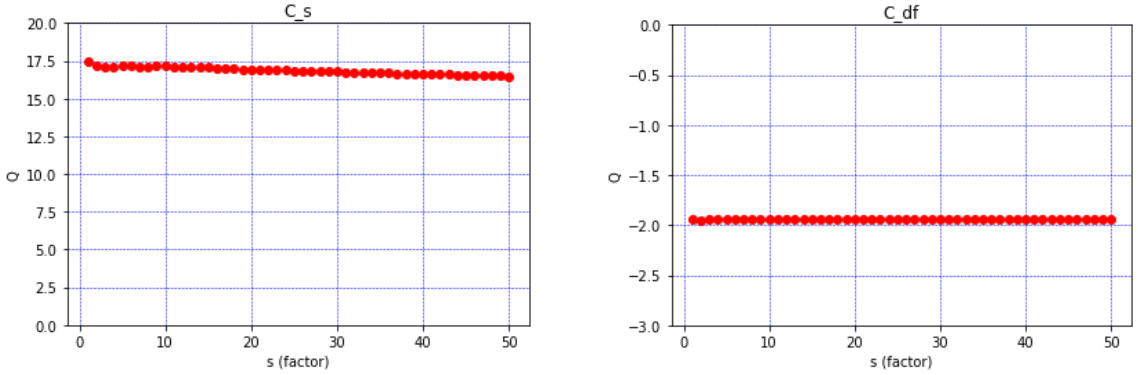

(a) C_s (b) C_{df}

Figure 21: *(s,Q) plot for third-order spherical aberration C_s in (21a) and defocus C_{df} in (21b) on the right. Initial $C'_s = 5$ mm and $C'_{df} = 0.01$ μm.*

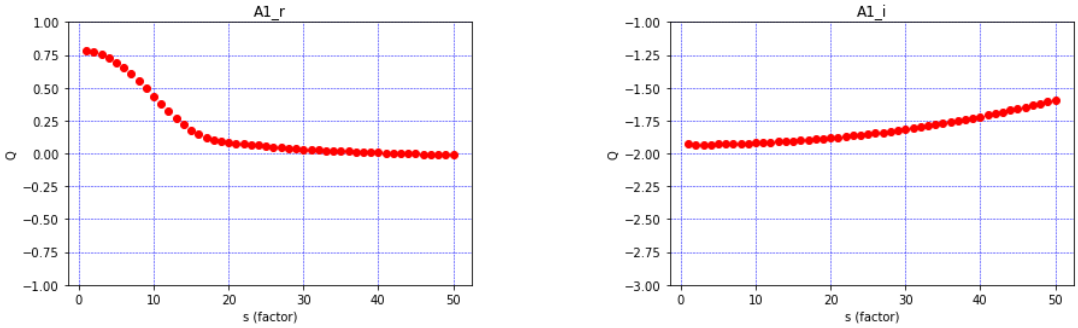

(a) $A_{1,r}$ (b) $A_{1,i}$

Figure 22: *(s,Q) plot for two-fold astigmatism A_1, with initial $|A'_{1,1}| = 0.01$ μm. On the left in (22a), the test for only real $A_{1,r}$, on the right in (22b) imaginary $A_{1,i}$.*

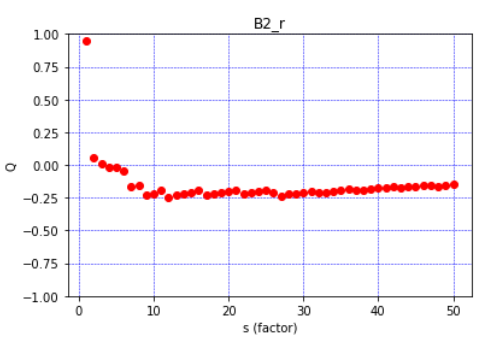

(a) $B_{2,r}$

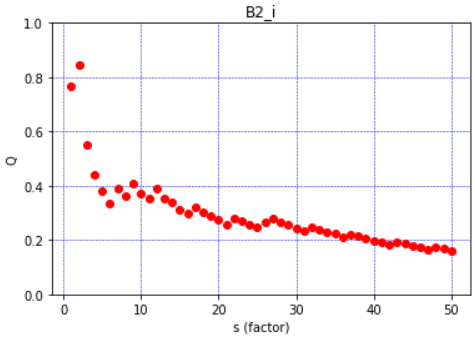

(b) $B_{2,i}$

Figure 23: *(s,Q) plot for second order coma B_2, with initial $|B'_{2,1}| = 0.2$ μm. On the left in (23a), the test for only real $B_{2,r}$, on the right in (23b), imaginary $B_{2,i}$.*

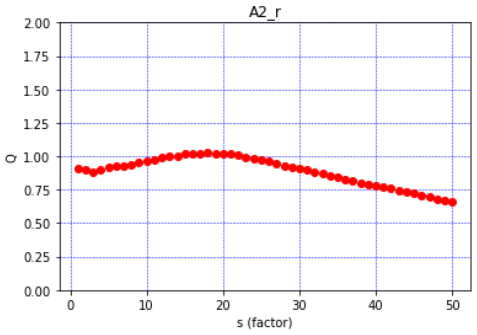

(a) $A_{2,r}$

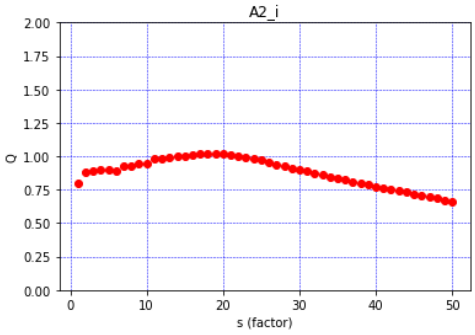

(b) $A_{2,i}$

Figure 24: *(s,Q) plot for three-fold astigmatism A_2, with initial $|A'_{2,1}| = 1$ μm. On the left in (24a), the test for only real $A_{2,r}$, on the right in (24b) imaginary $A_{2,i}$.*

Discussion

PSF extraction

The methods described in this report are largely based on the methods given in this article by Uno et al. (2005) [1]. Some adaptations were made to the methods based on foundings during the research. The article describes the convolution integral as follows:

$$\begin{aligned} h(x,y) &= \int_{-\infty}^{\infty}\int_{-\infty}^{\infty} f(u+x, v+y)g(u,v)\,\mathrm{d}u\,\mathrm{d}v + \gamma(x,y), \\ H(X,Y) &= F(X,Y)\overline{G(X,Y)} + \Gamma(X,Y), \end{aligned} \tag{22}$$

with $\overline{G(X,Y)}$ representing the complex conjugate of $G(X,Y)$. This differs from the representations in equations (1) and (2). Experimentally this resulted in the retrieved PSFs $g_{u,o}$ being rotated around its center by π rad when using both methods for PSF extraction. This is illustrated in figure (25). Figure (25a) shows the under- and over-focus PSFs extracted from the through-focus series shown in figure (9) by using equations (1) and (2). Below, (25b) shows the PSFs extracted from the same through-focus series, using the equations in (22). Finally, figure (25c) depicts the same PSFs shown in figure (25b), rotated over π rad.

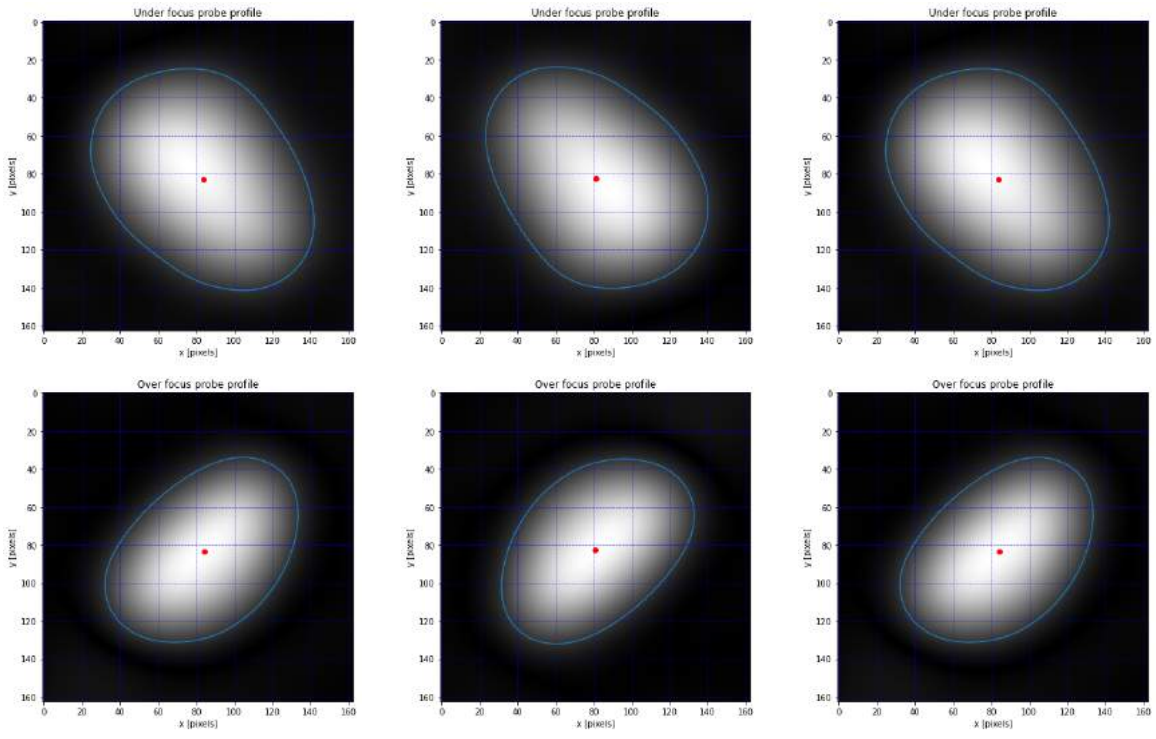

(a) (b) (c)

Figure 25: *Extracted under- and over-focus PSFs from the through-focus series shown in figure (9). On the left, (25a) shows the extracted under (first row) and over (second row) focus PSFs obtained by using equations (1) and (2). In the middle, (25b) shows the PSFs extracted from the same through-focus series, using the equations in (22). Finally, the right figure (25c) depicts the same PSFs as in (25b), rotated over* π rad.

A consequence of changing this definition is that the orientation of the original digitizations for some aberration coefficients is no longer accurate, but this only results in retrieved coefficients being rotated around a certain angle, which will be discussed next.

Rotation of the PSF

The rotation around π rad changes the orientation of some of the retrieved aberration coefficients. If the entire PSF is rotated around an angle α^*, then the angles θ_k of the profile lines drawn through the PSF are also rotated around the same angle. Indeed, let $\theta_k^* = \theta_k + \pi$, and define the aberration coefficients in Table 1 with this θ_k^*, we obtain the following digitizations for the aberration coefficients:

$$\begin{aligned}
C_{df}^* &= \frac{1}{N}\sum_{k=1}^{N}(\sigma_{u,k} - \sigma_{o,k})\exp\left(i0(\theta_k + \pi)\right) = C_{df}, \\
A_1^* &= \frac{2}{N}\sum_{k=1}^{N}(\sigma_{u,k} - \sigma_{o,k})\exp\left(i2(\theta_k + \pi)\right) = A_1\exp\left(i2\pi\right) = A_1, \\
B_2^* &= \frac{2}{N}\sum_{k=1}^{N}(\mu_{u,k} + \mu_{o,k})\exp\left(i(\theta_k + \pi)\right) = B_2\exp\left(i\pi\right) = -B_2, \\
A_2^* &= \frac{2}{N}\sum_{k=1}^{N}(\mu_{u,k} + \mu_{o,k})\exp\left(i3(\theta_k + \pi)\right) = A_2\exp\left(i3\pi\right) = -A_2, \\
C_s^* &= \frac{1}{N}\sum_{k=1}^{N}(\rho_{u,k} - \rho_{o,k})\exp\left(i0(\theta_k + \pi)\right) = C_s.
\end{aligned} \tag{23}$$

Added are the expressions for $\exp\left(i\alpha\theta_k\right)$ for C_{df} and C_s. These changes should be visible in the signs of the retrieved aberration coefficients. Table 5 shows the retrieved coefficients C_n^* from the under- and over-focus PSFs shown in figure (25a) on the left, and the coefficients C_n retrieved from the PSFs in figure (25b) on the right. Indeed, the coefficients for coma B_2 and A_2 change sign, though they are slightly shifted in value.

Table 5: *Retrieved coefficients C_n from the under- and over-focus PSFs shown in figure (25a) on the left, and the coefficients C_n^* retrieved from the PSFs in figure (25b) on the right.*

Aberration coefficients	C_n	C_n^*	O **(in** m**)**
C_{df}	4.325	4.247	10^{-8}
A_1	$0.07360 + 9.284i$	$0.07635 + 9.019i$	10^{-8}
B_2	$-0.6404 + 0.8262i$	$2.593 - 0.3950i$	10^{-7}
A_2	$-1.241 + 1.469i$	$1.207 - 1.685i$	10^{-6}
C_s	-1.081	-1.185	10^{-3}

Contours, cropping, and centroids

First, the extracted PSFs $|g_{u,o}|$ are cropped. This cropping process influences the number of points M selected on the profile line. Next, contours $C_{u,o}$ are drawn around the shape of the PSF. Finally, the centroids $(x_{u,0}, y_{u,0})$ and $(x_{o,0}, y_{o,0})$ of the shape based on the contours are calculated. The reference article [1] did not include this process, in this research it served well as a check for the probe shape extraction. Furthermore, the reference article did not specify which 'center of the probe' [1] was meant: the topological center of the probe or the weighted center of the probe (the coordinate located on the average of all intensity points p_j). The first of these two was assumed in this report. The development of a similar method using the weighted center of the probe is therefore suggested. Another recommendation is to select the number of points on each profile line as a measure of the contour, instead of the image size.
The setting of $p_j = 0$ for $p_j \notin C_{u,o}$ was a good measure for the spot shape. However, for one test aberration coefficient A_1, this resulted in the exclusion of some outside points with values $p_j \geq 0.2$. This is shown in figure (26). The extracted under-focus PSF for real $A_{1,r}$ is shown in the left column and imaginary $A_{1,i}$ in the right column (see figures (A.14a) and (A.15a) in the Appendix, section on *Two-fold astigmatism*), with four profile lines for $k = 0, 20, 40, 80$. Below these PSFs, two plots depicting the same profile lines are shown: in the middle row (figures (26c) and (26d)) the profile lines using the exclusion of all $p_j \leq 0.2$ is shown. In the final row (figures (26e) and (26f)) the same lines without the exclusion of points outside the contour. It can be seen that certain points $p_j \geq 0.2$ are excluded in (26c) that are included in figure (26e). However, this issue does not present itself for the imaginary two-fold astigmatism test. In figure (26d) it can be seen that the exclusion of points $p_j < 0.2$ is implemented successfully. Further research into the use of this contour tracing and exclusion of points outside the contours is recommended.

Characteristics

The three characteristics used for calculating the aberration coefficients all represent a certain property of the normalized PSFs they are extracted from. Below they are discussed.

Asymmetry

Asymmetry μ has the same representation as the mean of a discrete probability density function. It is due to this definition that extra research into comparing these characteristics to properties of probability density functions was done.

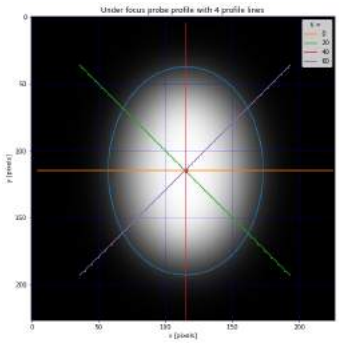

(a) *Under focus PSF depicting $A_{1,r}$, with four profile lines.*

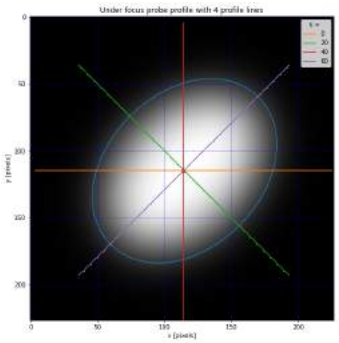

(b) *Under focus PSF depicting $A_{1,i}$, with four profile lines.*

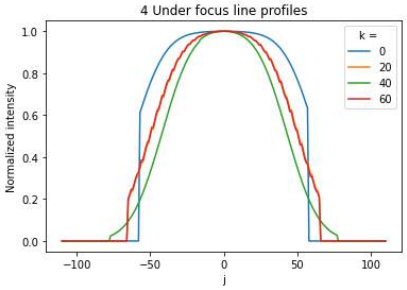

(c) *$A_{1,r}$ with contour exclusion.*

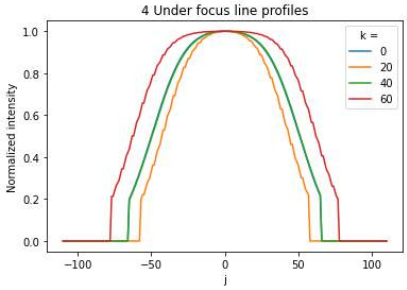

(d) *$A_{1,i}$ with contour exclusion.*

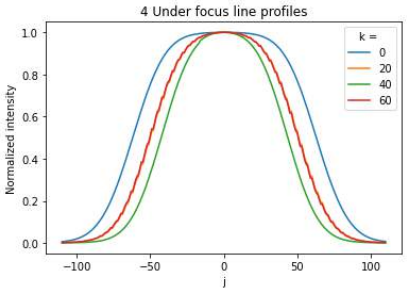

(e) *$A_{1,r}$ with contour exclusion.*

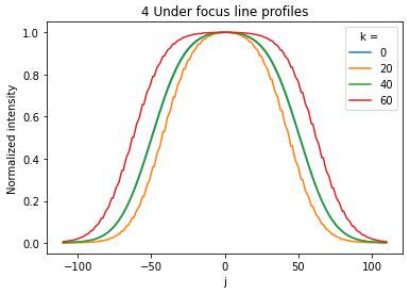

(f) *$A_{1,i}$ with contour exclusion.*

Figure 26: *Figure depicting the extracted PSFs depicting two-fold astigmatism. It can be seen that certain points $p_j \geq 0.2$ are excluded in (26c) that are included in figure (26e). However, this issue does not present itself for the imaginary two-fold astigmatism test. In figure (26d) it can be seen that the exclusion of points $p_j < 0.2$ is implemented successfully.*

Width

The width characteristic σ has a slightly different representation in the article compared to this report:

$$\sigma = \sqrt{\frac{1}{W}\sum_j j^2 p_j}, \tag{24}$$

In statistics, the expression for $\frac{1}{W}\sum_j j^2 p_j$ represents the second order moment of a distribution. Very little motivation is given for this expression, which most likely used the assumption that $\mu = 0$ in the expression found in equations (13). A fairly reasonable assumption, since the mean μ is often located very close to $j = 0$ compared to the size of the line profile. Still, because μ is

calculated anyway, it made sense to use the proper statistical definition of standard deviation. No information is lost between the two definitions, just a slight shift. This is illustrated best by coma B_2, as it is an aberration defined by its asymmetry $\mu \neq 0$. Figure (27) depicts the PSFs from figure (A.24a), with four profile lines for $k = 0, 20, 40, 60$ drawn through its centroid. Below them is a plot of the same profile lines, and finally a plot of the two definitions of width σ from equations (13) and (24) for each k, together with a plot of the difference. This is done for under-focus.

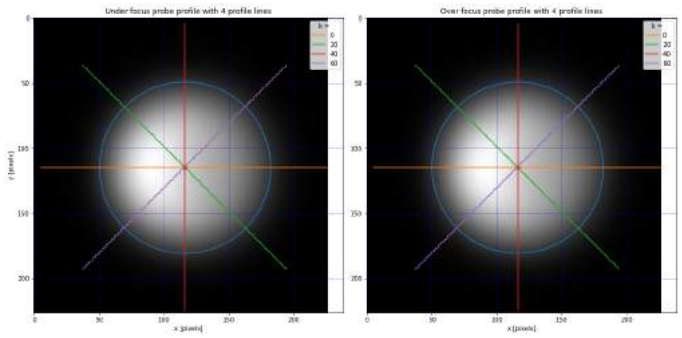

(a) *Extracted PSFs from figure (A.24a), with profile lines for* $k = 0, 20, 40, 60$.

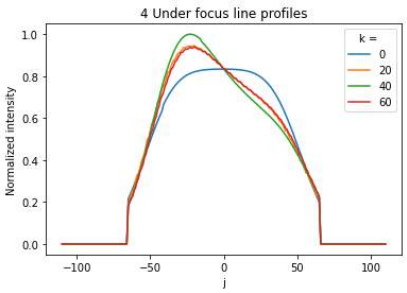

(b) *Profile lines for* $k = 0, 20, 40, 60$.

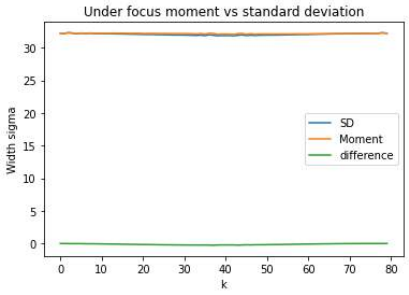

(c) *Definitions of* σ *with their difference.*

Figure 27: *PSFs from figure (A.24a), with four profile lines for* $k = 0, 20, 40, 60$ *drawn through its centroid in (27a). Below them are plots of the same profile lines in (27b), and finally plots of the two definitions of width* σ *from equations (13) and (24) for each* k*, together with a plot of the difference in (27c). This is done for under-focus. Indeed, there is very little difference between the* σ *calculated with equation (24) and the* σ *that uses (13).*

Curvature

The curvature characteristic ρ is the only characteristic in the retrieval method that does not directly represent a statistical property, unlike asymmetry μ, equivalent to the mean and width σ representing the standard deviation. Some research into statistical equivalents did not result in anything directly relatable to the curvature definition. It is recommended to continue research into this characteristic, as it does seem to somewhat accurately describe the effect spherical aberration has on the PSF of an optical system.

Aberration coefficients

The five aberration coefficients presented in this report are defined as average differences between characteristics of the under- and over-focus PSFs $|g_{u,o}|$, except B_2 and A_2. The coefficients are discussed in order of appearance.

Defocus

Due to the rotational symmetry of this aberration, the rotation of the retrieved PSFs around π rad is of no consequence to the final digitized C_{df}. Positive C_{df} indicates that the sample is located further away from the objective lens than the focal plane. It is therefore recommended that the definition of defocus C_{df} [1] should be multiplied by -1. A positive defocus coefficient C_{df} means that the under-focus PSF g_u has a lower width σ than the over-focus PSF g_o, causing the coefficient defined in Table 1 to be the negative of the actual defocus coefficient.

Two-fold astigmatism

The signs of the retrieved real $A_{1,r}$ aberration coefficients match the signs of the input coefficients $A'_{1,r}$, the retrieved imaginary $A_{1,i}$ is of opposite sign to the initial $A'_{1,i}$, one suggestion would be to replace the original digitization presented in Table 1 with its complex conjugate. This would in hindsight align the argument of A_1 with the argument of A'_1. The digitized definition of A_1 described in Table 1 seems to correctly determine the highest magnitude between the real and imaginary parts of A_1. This suggests that the definition of A_1 is a representative computational method for this aberration coefficient. However, the (s, Q) plot did not show a constant Q for a factorized increase in simulated A'_1. Additionally, the contour excluded some points p_j that should have been included. Further research into the viability of this contour tracing and exclusion method is therefore recommended.

Second-order Coma

In the PSFs $g_{u,o}$, the effect of coma results in a skewed intensity distribution, which in turn results in asymmetry $\mu \neq 0$. Furthermore, the effect of coma is the same for under- and over-focus, see figure (7), so for the definition of B_2, the average sum of the under- and over-focus characteristics $\mu_{o,u}$ is calculated instead of the average difference. We see this done as well for three-fold astigmatism A_2. The rotation of the extracted PSF due to omitting the complex conjugate signs on the functions, originally found in [1] and defined in equation (22) also influences the orientation of the retrieved coefficients. The retrieved coefficients B_2 do not match the input of the PSFs used to generate the effects of coma. When there is only real simulated B'_2, the digitization results in a largely imaginary B_2, and the opposite is true as well. This suggests an incorrect digitization of B_2, or an incorrect representation in the PSF simulation. Further research into the retrieval of coma B_2 is recommended, specifically in the retrieval of the argument of the coefficient. One suggestion would be to multiply the digitization of B_2 with $\exp(i\frac{\pi}{2})$ in Table 1. This simple solution aligns the retrieved coefficients for coma B_2 with the orientation of B'_2. Additionally, due to the mismatch of magnitudes of the retrieved coefficients, it is not possible to confirm consistency out of the (s, Q) plot.

Three-fold astigmatism

For its definition, A_3 is calculated with the average sum of the under- and over-focus characteristics $\mu_{u,o}$. This definition for three-fold astigmatism scales consistently with an increase in A_2, both real and imaginary. Like B_2, the retrieved coefficients A_2 do not match the input coefficients, though more than coma. The sign of the retrieved coefficient is accurate, but the magnitude of the retrieved A_2 seems to favor the imaginary part when the input coefficient is real, and vice versa. This once again suggests an incorrect digitization of A_2 or an incorrect representation of A_2 in the PSF simulation. One suggestion, like with B_2, is to multiply the digization of A_2 with $\exp(i\frac{\pi}{2})$ to match the orientation of A_2'.

Third-order spherical aberration

Third-order spherical aberration is the most important aberration discussed in this report, as the SEM of the ImPhys department has a spherical aberration corrector, and it is the most prominent aberration in SEM measurements. The digitization seems to correctly determine whether there is a large amount of spherical aberration, though the exact magnitude of the retrieved C_s is not accurate. There is a difference of around factor 2 between the retrieved coefficient from the simulated PSFs $g'_{u,o}$ and the coefficient from the extracted PSFs $g_{u,o}$, see figure see figure (20). This can be explained when taking a look at the profile lines drawn through both the simulated PSFs (see figure (28)) and extracted PSFs (figure (18)). There is a significant decrease in the difference between the intensity of the center of the PSFs. This results in a lower digitized

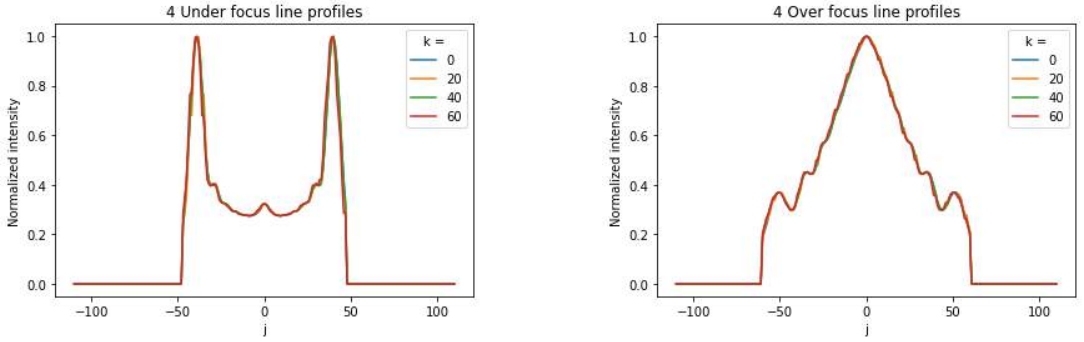

(a) *Under-focus simulated PSF for C_s'.* (b) *Over-focus simulated PSF for C_s'*

Figure 28: *Profile lines for $k = 0, 20, 40, 60$ of the simulated PSFs in figure (17b), $C_s' = 5$ mm. When compared to the extracted PSF profile lines depicted in figure (19), it is clear that there is a difference in the intensity of the center of the PSF and the overall intensity distribution of the PSF. This results in a decrease in digitized C_s after extracting the PSFs from a through-focus series.*

C_s value. The retrieval method still extracts C_s as the largest contributing coefficient. Further research into the exact identity of ρ and the digitization C_s is recommended, specifically how this ρ of a line profile scales with increasing and decreasing defocus. This will determine if this characteristic accurately represents the effect of spherical aberration C_s.

Conclusion

In this report, the process of aberration coefficient retrieval from a through-focus series of SEM images was assessed and tested. This process consisted of three parts: probe shape extraction, PSF analysis, and aberration coefficient calculation, which included a consistency test.

Probe shape extraction

The probe shape extraction method from a through-focus series of images is successfully described and implemented using Fourier analysis. The method originally described in [1] and stated in equations (22) uses complex conjugate signs in its definition of the image formation and extraction method, which resulted experimentally in probe shapes rotated over π rad. This rotation resulted in the digitization of B_2 and A_2 changing signs, no significant change was noted for the other three test aberration coefficients. Furthermore, the shapes of simulated PSFs convolved with a test image were successfully retrieved, as the retrieved probe shapes match the shapes of the PSFs used to create a simulated through-focus series. This extraction method was possible due to the approximation of an Airy pattern with a Gaussian function with mean $\mu_{Airy} = 0$ and standard deviation $\sigma_{Airy} = 0.689 r_{Airy}$.

PSF analysis

The analysis of these extracted PSFs using line profiles and characteristics had mixed results. The first two characteristics presented in [1] have been successfully identified as the mean μ and standard deviation σ of a probability density function with mass function p_j/W. The third (and arguably most important) characteristic curvature ρ has no such statistical equivalent. However, it could be inferred that ρ is a good measure of the effect of third-order spherical aberration. Further research into the exact identity of this ρ is recommended; specifically how this ρ of a line profile scales with increasing and decreasing defocus, to determine how accurate this characteristic is for representing the effect of spherical aberration C_s.
Using the diffraction integral, and the wave-optical description of an aberrated phase function Φ, PSFs representing the effects of singular aberrations were simulated and used as test samples for the aberration retrieval method.
Contour tracing around the retrieved PSFs had mixed results. For all aberrations, it presented a good measure of the spot shape. The implementation of an algorithm that excluded points p_j outside the contour was not accurate for one test aberration: two-fold astigmatism A_2. The contour tracing algorithm excludes important parts of the shapes of the PSFs.

Aberration coefficient calculation

The values of the retrieved aberration coefficients C_n did not match the simulated coefficients C'_n in magnitude. One explanation for these differences would be a mismatch in PSFs when generating a PSF and retrieving a PSF in terms of size and intensity distribution. A general recommendation is to continue research into comparing simulated aberration coefficients and

retrieved coefficients.
From the (s, Q) plots, the consistency of this described method of aberration retrieval can be suggested for three of the five test aberrations: defocus C_{df}, three-fold astigmatism A_2 and third-order spherical aberration C_s. For coma B_2 and two-fold astigmatism A_1, such a conclusion could not be made.
Defocus C_{df} is consistently negative when the simulated C'_{df} is positive and vice versa. A suggestion would be to multiply the digitization of C_{df} with -1 to match its input.
Retrieved two-fold astigmatism A_1 does not match the argument of the simulated input, further research into the scaling of two-fold astigmatism A_1 is recommended.
Coma B_2 does not match the input coefficients in both argument and magnitude. The difference in argument can be remedied by multiplying the digitization of B_2 with $\exp(i\frac{\pi}{2})$. Three-fold astigmatism A_2 does not match the argument of the simulated coefficient A'_2, and is not retrieved as the largest aberration coefficient in the simulations. More detailed research into the viability of asymmetry μ as characteristic for B_2 and A_2 is therefore suggested. Third-order spherical aberration does match the simulated coefficient C'_s in sign, but not in magnitude. There is a difference of around factor 2 between the retrieved coefficient from the simulated PSFs $g'_{u,o}$ and the coefficient from the extracted PSFs $g_{u,o}$. There is a significant decrease in the difference between the intensity of the center of the PSFs. The method still retrieves C_s as the largest aberration coefficient when analysing PSFs that depict only spherical aberration.
Furthermore, the coefficient Q diverges for larger values of s. One explanation for this is the contour tracing. As the effect of spherical aberration increases, the intensity values of the normalized over-focus PSF decrease, and as such more intensity points are left out of the spherical aberration calculation. Continued research into the digitization of spherical aberration with curvature ρ is suggested.

References

[1] Shinobu Uno, Kazuhiro Honda, Natsuko Nakamura, Miyuki Matsuya, and Joachim Zach. Aberration correction and its automatic control in scanning electron microscopes. *Optik 116*, 2005.

[2] https://en.wikipedia.org/wiki/Diffraction-limited_system. Accessed: 24-11-2023.

[3] https://www.thermofisher.com/blog/materials/what-is-sem-scanning-electron-microscopy-explained/. Accessed: 24-4-2024.

[4] https://en.wikipedia.org/wiki/Everhart%E2%80%93Thornley_detector. Accessed: 24-4-2024.

[5] https://www.hitachi-hightech.com/global/en/products/microscopes/sem-tem-stem/sem/su3800.html. Accessed:24-4-2024.

[6] Martin Oral and Bohumila Lencová. *Calculation of aberration coefficients by ray tracing*. Technical report, Institute of Scientific Instruments, Academy of Sciences of the Czech Republic, 2009.

[7] David C. Joy. *The Aberration Corrected SEM*. *American Institute of Physics*, 2005.

[8] Fumio Hosokawa, Hidetaka Sawada, Yukihito Kondo, Kunio Takayanagi, and Kazumoto Suenaga. *Development of Cs and Cc correctors for transmission electron microscopy*. Technical report, Department of Condensed Matter Physics, Tokyo Institute of Technology, 2013.

[9] Hideto Dohi and Pieter Kruit. *Design for an aberration corrected scanning electron microscope using miniature electron mirrors*. Technical report, Faculty of Applied Sciences, TU Delft and Hitachi High-Technologies Corporation, 2018.

[10] Matthew D. Zotta, Mandy C. Nevins, Richard K. Hailstone, and Eric Lifshin. *The Determination and Application of the Point Spread Function in the Scanning Electron Microscope*. *Microscopy and Microanalysis*, 2018.

[11] *Thorlabs resolution test targets*. https://www.thorlabs.com/newgrouppage9.cfm?objectgroup_id=4338. Accessed: 13-05-2024.

[12] *Airydisk Wikipedia page*. https://en.wikipedia.org/wiki/Airy_disk. Accessed: 11-05-2024.

[13] Rolf Erni. *Aberration-corrected Imaging in Transmission Electron Microscopy - An Introduction*, chapter 7. Imperial College Press, 2010.

[14] Joseph J.M. Braat, Peter Dirksen, Sven van Haver, and Augustus J.E.M. Janssen. *Detailed description of the ENZ approach*. https://nijboerzernike.nl/. Accessed: 25-4-2024.

[15] https://en.wikipedia.org/wiki/Multimodal_distribution. Accessed: 25-6-2024.

[16] *Calibration standards and specimens, Agar Scientific*. Accessed: 23-05-2024.

[17] https://en.wikipedia.org/wiki/Hann_function. Accessed: 25-6-2024.

[18] *Understanding FFT Windows, Michigan State University*. Accessed: 06-06-2024.

[19] Contour tracing function. https://scikit-image.org/docs/stable/api/skimage.measure.html. Accessed: 23-05-2024.

Appendix

Introduction

The figures depicting the simulated through-focus series, extracted PSFs, retrieved aberration coefficients, and (s, Q)-plot images mentioned in the section on Results are depicted in the following subsections for spherical aberration C_s, defocus C_{df}, two-fold astigmatism A_1, coma B_2 and three-fold astigmatism A_2.
Figure (A.1) depicts the windowed gold on carbon test image that serves as the just focus image h (left), along with the just focus PSF g (right). For each aberration mentioned above,

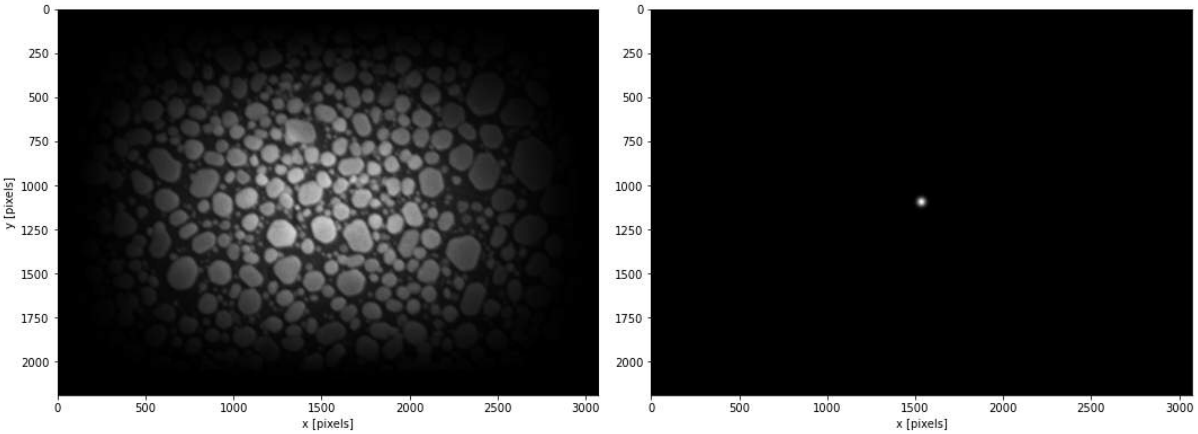

Figure A.1: *Windowed image depicting the gold on carbon test image that serves as just focus image h on the left. On the right, the assumed just focus PSF g is shown, as defined in the results, see figure (17).*

this image h is convolved with simulated under and over-focus PSFs $g'_{u,o}$ simulating exactly one of the five discussed aberrations, using the diffraction integral (see equation (11)) to simulate a through-focus series $h_{u,o}$. The two PSFs each have defocus $C_{df} = \pm 1\ \mu\mathrm{m}$. The simulated under and over-focus images $h_{u,o}$ are depicted on the left, together with the PSFs $|g'_{u,o}|$ used to create the images on the right. For each pair of images and PSFs, under focus is shown left, and over focus on the right. All images are depicted in pixels on x and y axis.

Next, using equations (5) and (6), the under and over-focus PSFs $g_{u,o}$ are extracted and compared to the shape of the simulated PSFs $g'_{u,o}$. The reference just focus PSF g is again assumed to be a Gaussian as described in equation (8), with Airy radius assumed $r_{Airy} = 20\ \mathrm{nm}$. Their centroids $(x_{u,0}, y_{u,0})$, $(x_{o,0}, y_{o,0})$ and contours $C_{u,o}$ are plotted in the same image as well.

The aberration coefficient retrieval method is then applied to the simulated PSFs $g'_{u,o}$ and the extracted PSFs $g_{u,o}$. The resulting aberration coefficient magnitudes are shown in bar plots, with blue representing the coefficients extracted from $g'_{u,o}$ and orange the extracted coefficients from $g_{u,o}$.

Lastly, five images for $s = 10, 20, 30, 40, 50$ that serve as samples for the (s, Q) plots in the section on Results are shown with the contours and centroids.

Spherical aberration

Through-focus series

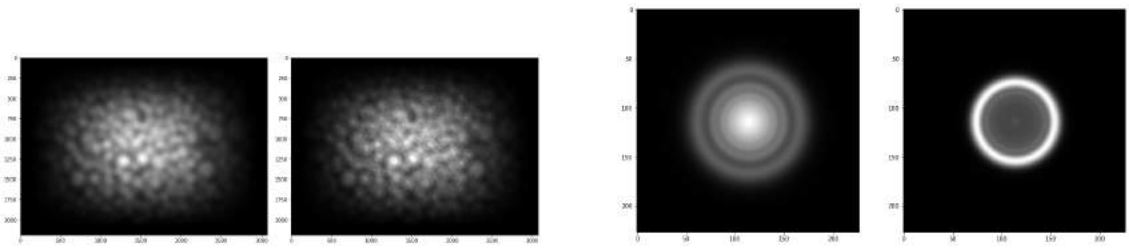

(a) *Simulated images* $h_{u,o}$ (b) *Simulated PSFs* $|g'_{u,o}|$

Figure A.2: *Spherical aberration:* $C_s = -5$ mm

PSF extraction

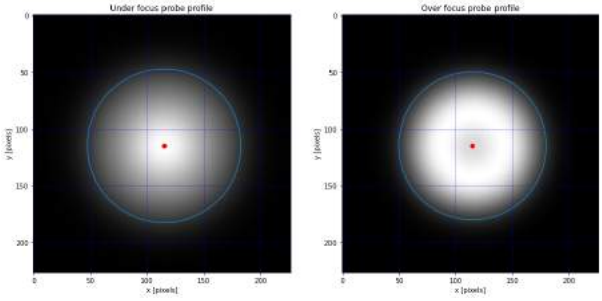

Figure A.3: *Extracted PSFs* $|g_{u,o}|$ *from the images in figure (A.2a).*

Retrieved aberration coefficients

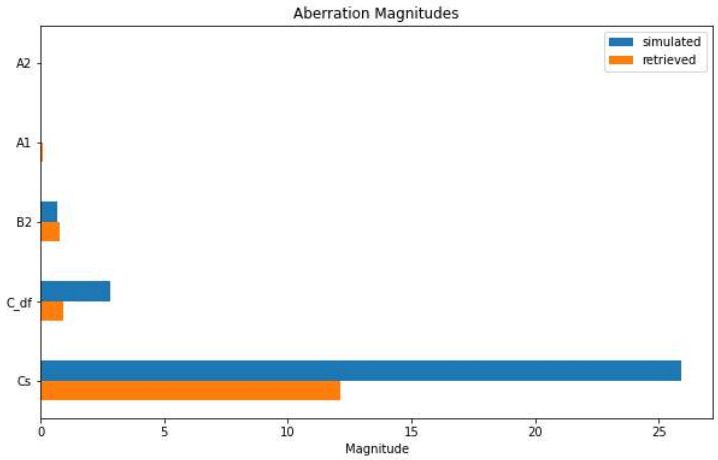

Figure A.4: *Barplot depicting the moduli of the extracted aberration coefficients in blue for the PSFs in figure (A.2) and orange for the PSFs in figure (A.3).*

Defocus

Through-focus series

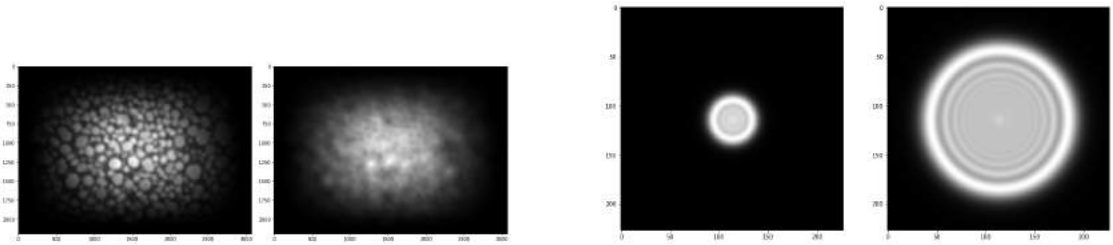

(a) *Simulated under and over focus images* $h_{u,o}$ (b) *Simulated PSFs* $|g'_{u,o}|$

Figure A.5: *Defocus* $C'_{df} = 0.5\ \mu\mathrm{m}$

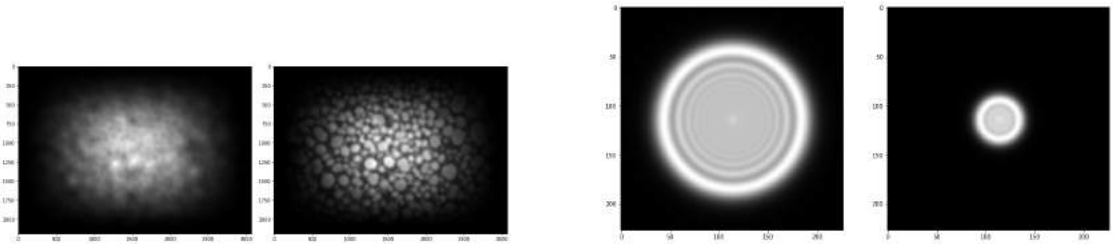

(a) *Simulated under and over focus images* $h_{u,o}$ (b) *Simulated PSFs* $|g'_{u,o}|$

Figure A.6: *Defocus* $C'_{df} = -0.5\ \mu\mathrm{m}$

PSF extraction

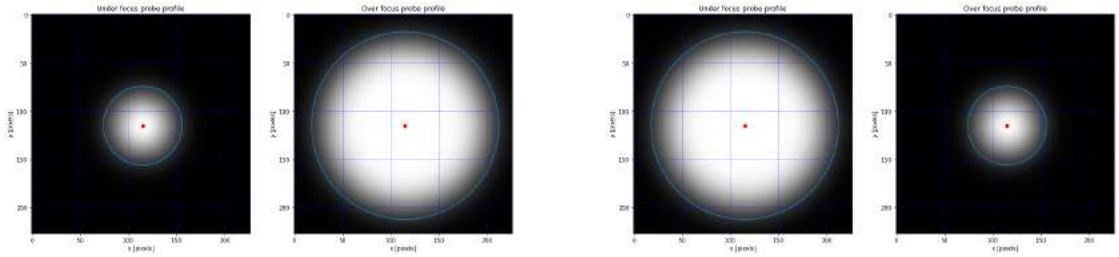

(a) (b)

Figure A.7: *Extracted PSFs* $|g_{u,o}|$ *from the images in figures (A.5a) on the left and (A.6a) on the right.*

Retrieved aberration coefficients

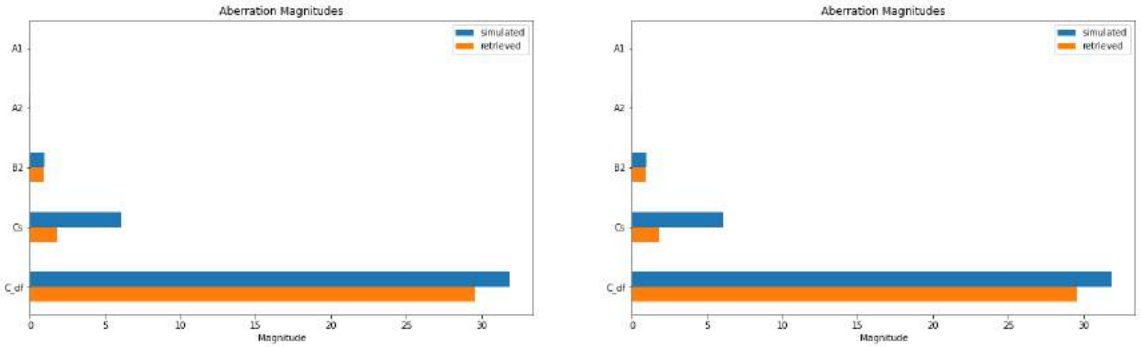

(a) $C'_{df} = 0.5\ \mu\text{m}$ (b) $C'_{df} = -0.5\ \mu\text{m}$

Figure A.8: *Defocus*

(s,Q) plot sample images

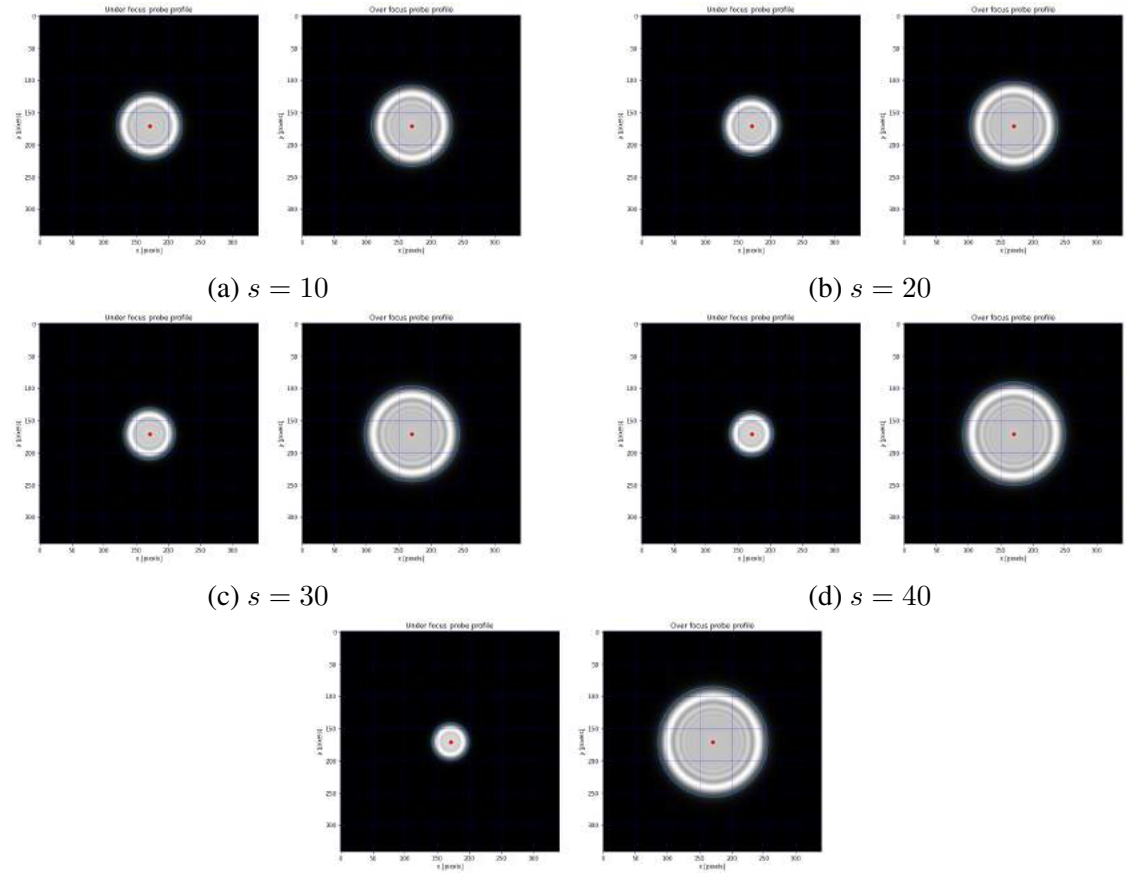

(a) $s = 10$ (b) $s = 20$

(c) $s = 30$ (d) $s = 40$

(e) $s = 50$

Figure A.9: *Simulated PSFs imitating spherical aberration with coefficients* $C'_{df,s} = sC_{df,1}$, $C'_{df,1} = 0.01\ \mu\text{m}$, *see Table 4. The PSFs are shown for* $s = 10, 20, 30, 40, 50$.

Two-fold astigmatism

Through-focus series

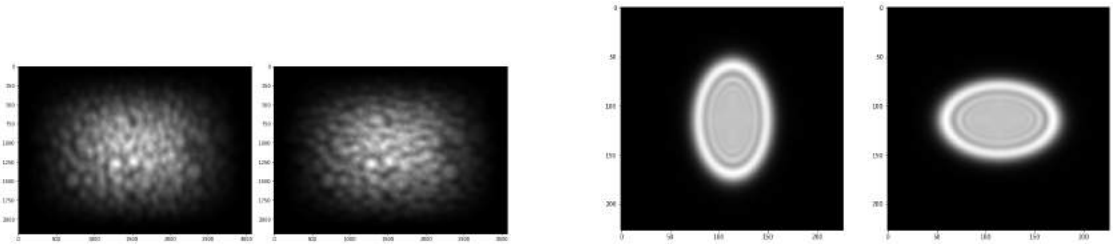

(a) *Simulated under and over focus images* $h_{u,o}$ (b) *Simulated PSFs* $|g'_{u,o}|$

Figure A.10: *Two-fold astigmatism* $A'_{1,r} = 0.2\ \mu\text{m}$, $A'_{1,i} = 0$

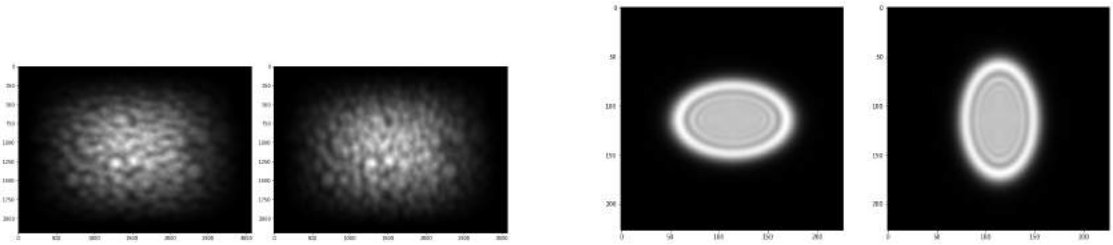

(a) *Simulated images* $h_{u,o}$ (b) *Simulated PSFs* $|g'_{u,o}|$

Figure A.11: *Two-fold astigmatism:* $A'_{1,r} = -0.2\ \mu\text{m}$, $A'_{1,i} = 0$

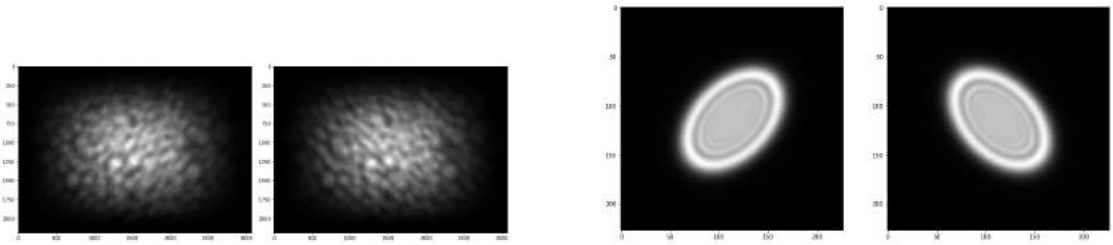

(a) *Simulated images* $h_{u,o}$ (b) *Simulated PSFs* $|g'_{u,o}|$

Figure A.12: *Two-fold astigmatism:* $A'_{1,r} = 0$, $A'_{1,i} = 0.2\mu\text{m}$

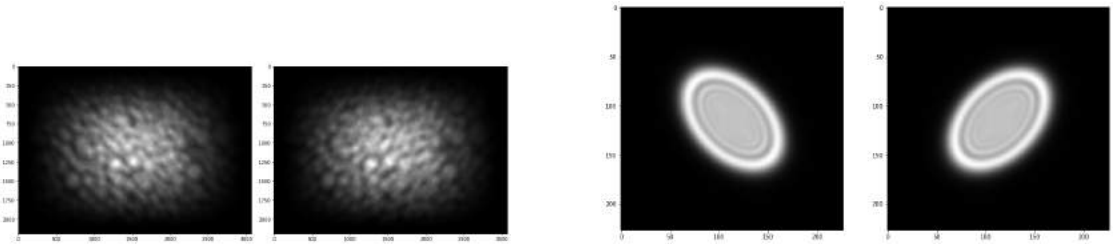

(a) *Simulated images* $h_{u,o}$ (b) *Simulated PSFs* $|g'_{u,o}|$

Figure A.13: *Two-fold astigmatism:* $A'_{1,r} = 0$, $A'_{1,i} = -0.2\mu\text{m}$

PSF extraction

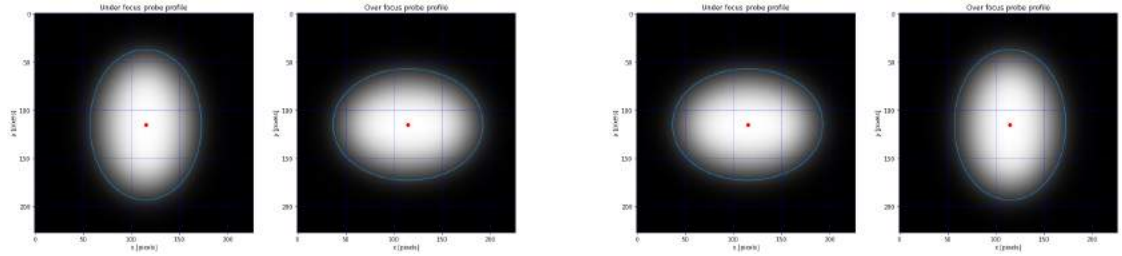

(a) (b)

Figure A.14: *Extracted PSFs $|g_{u,o}|$ from the images in figures (A.10a) on the left and (A.11a) on the right.*

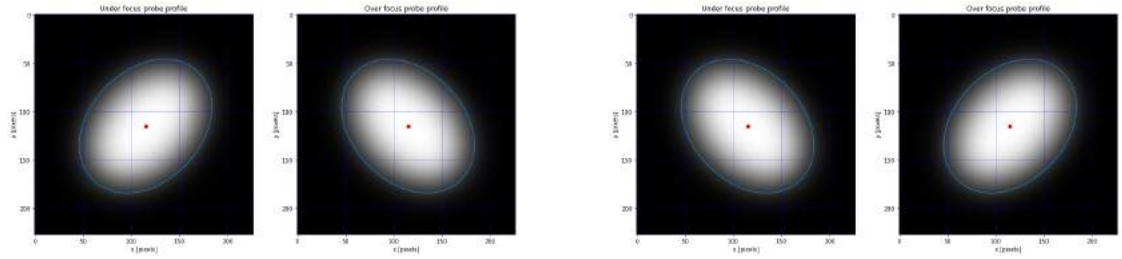

(a) (b)

Figure A.15: *Extracted PSFs $|g_{u,o}|$ from the images in figures (A.12a) on the left and (A.13a) on the right.*

Retrieved aberration coefficients

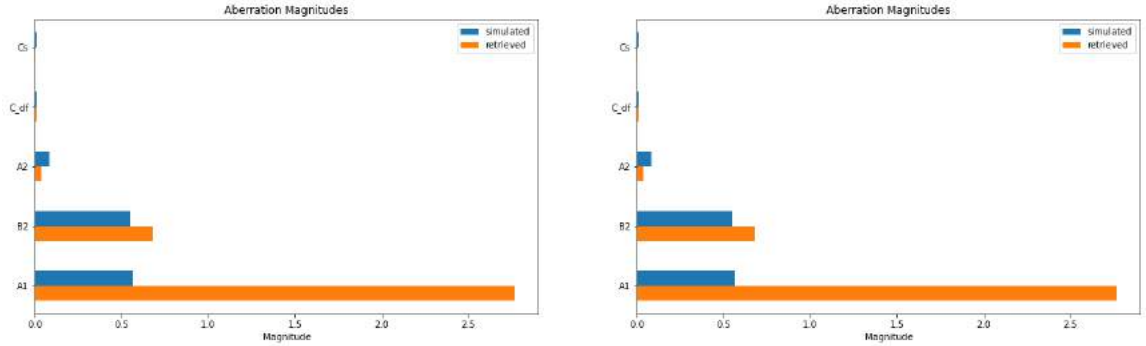

(a) $A'_{1,r} = 0.2\ \mu\text{m}$, $A'_{1,i} = 0$ (b) $A'_{1,r} = -0.2\ \mu\text{m}$, $A'_{1,i} = 0$

Figure A.16: *Two-fold astigmatism, real*

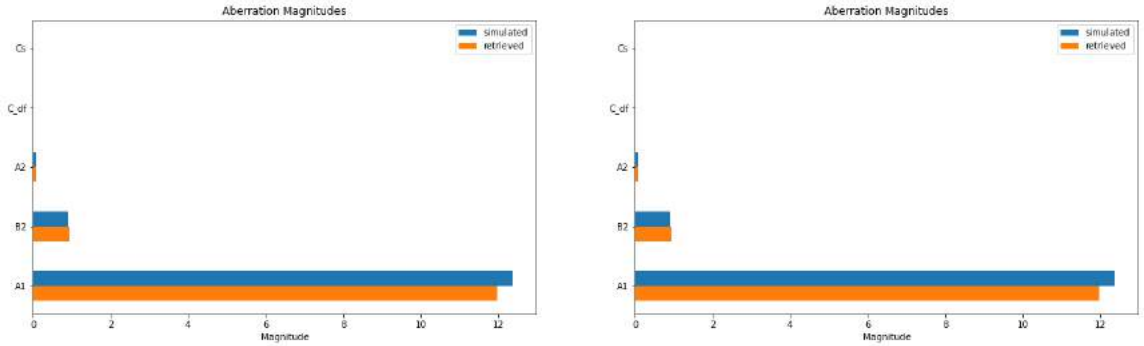

(a) $A'_{1,r} = 0$, $A'_{1,i} = 0.2$ μm (b) $A'_{1,r} = 0$, $A'_{1,i} = -0.2$ μm

Figure A.17: *Two-fold astigmatism, imaginary*

(s,Q) plot sample images

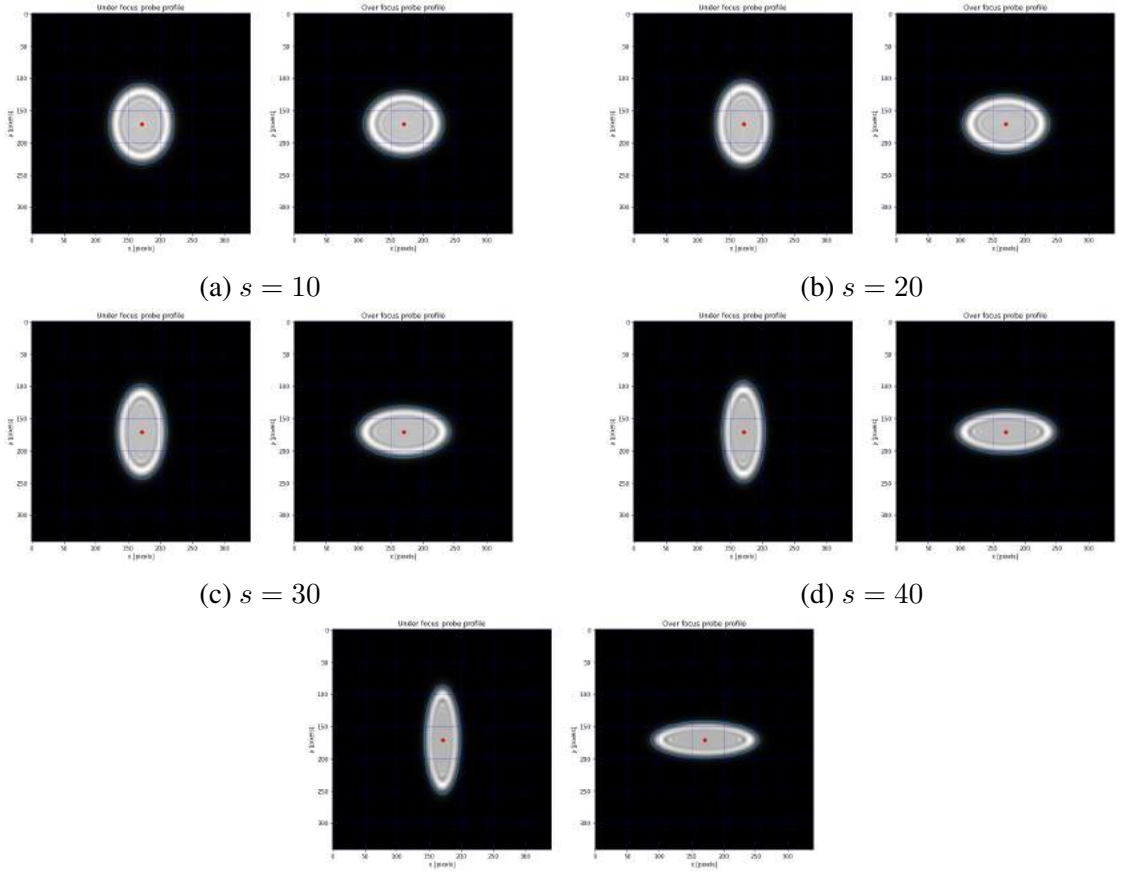

(a) $s = 10$ (b) $s = 20$

(c) $s = 30$ (d) $s = 40$

(e) $s = 50$

Figure A.18: *Simulated PSFs imitating spherical aberration with coefficients* $A'_{1,r,s} = sA'_{1,r,1}$, $A'_{1,r,1} = 0.01$ μm*, see Table 4. The PSFs are shown for* $s = 10, 20, 30, 40, 50$.

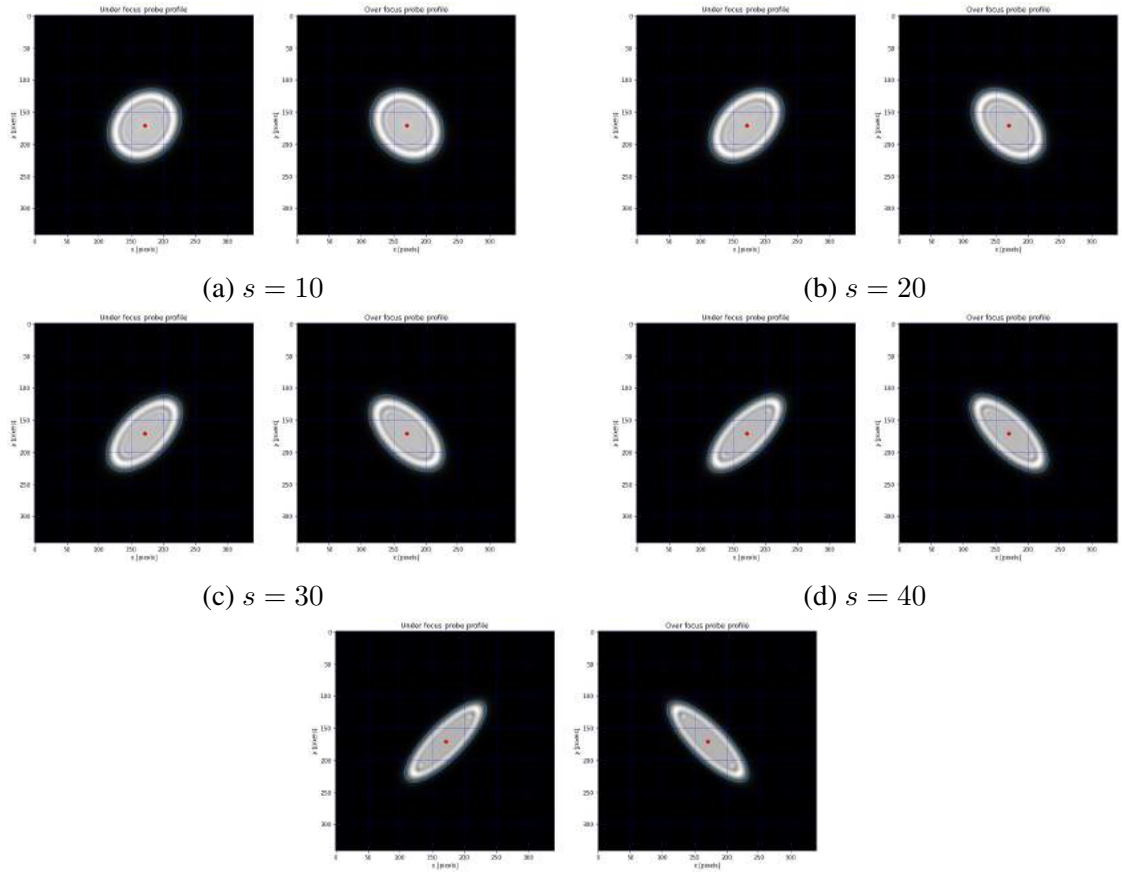

(a) $s = 10$ (b) $s = 20$

(c) $s = 30$ (d) $s = 40$

(e) $s = 50$

Figure A.19: *Simulated PSFs imitating spherical aberration with coefficients* $A'_{1,i,s} = sA'_{1,i,1}$, $A'_{1,i,1} = 60\ \mu\text{m}$*, see Table 4. The PSFs are shown for* $s = 10, 20, 30, 40, 50$.

Coma

Through-focus series

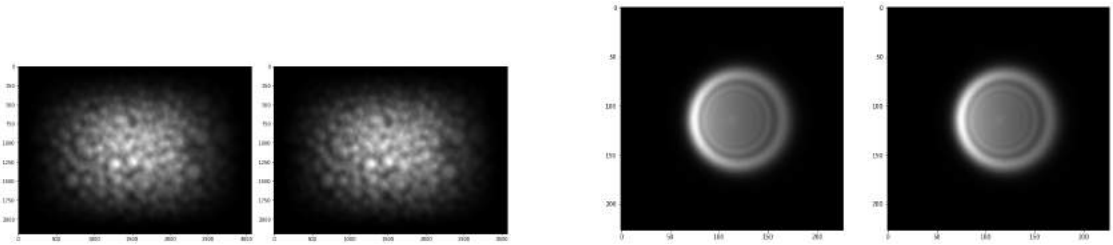

(a) *Simulated images* $h_{u,o}$ (b) *Simulated PSFs* $|g'_{u,o}|$

Figure A.20: *Coma:* $B'_{2,r} = 8\ \mu\text{m}$, $B'_{2,i} = 0$

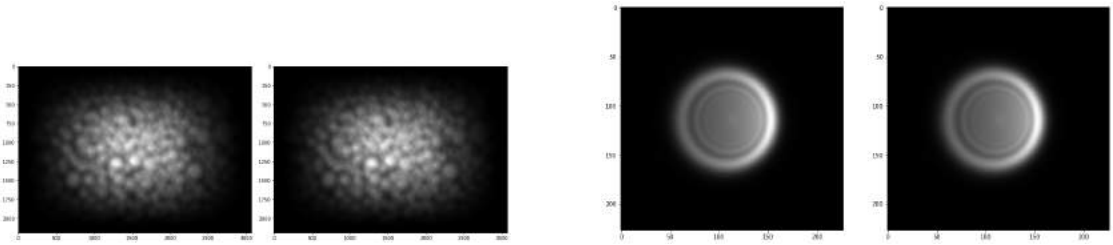

(a) *Simulated images* $h_{u,o}$ (b) *Simulated PSFs* $|g'_{u,o}|$

Figure A.21: *Coma:* $B'_{2,r} = -8\ \mu\text{m}$, $B'_{2,i} = 0$

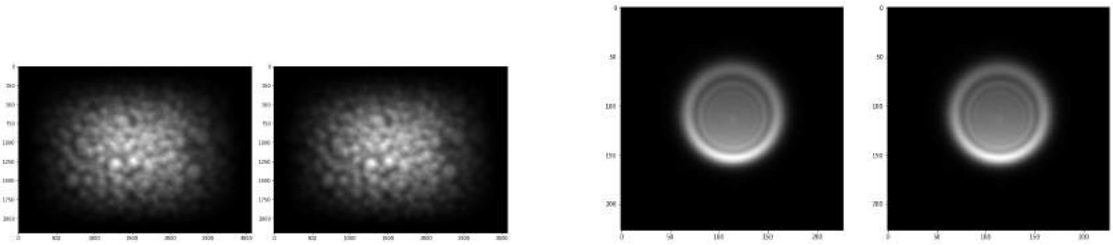

(a) *Simulated images* $h_{u,o}$ (b) *Simulated PSFs* $|g'_{u,o}|$

Figure A.22: *Coma:* $B'_{2,r} = 0$, $B'_{2,i} = 8\ \mu\text{m}$

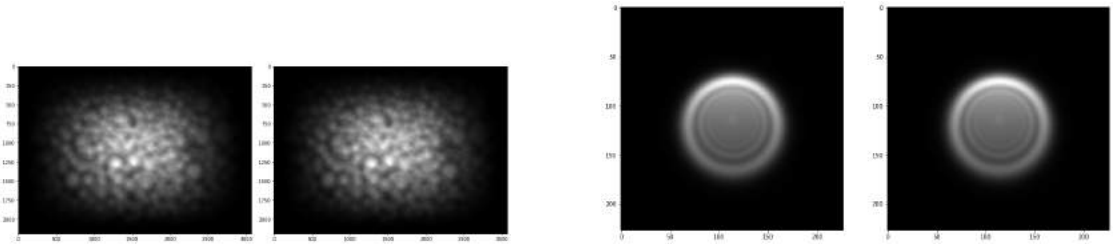

(a) *Simulated images* $h_{u,o}$ (b) *Simulated PSFs* $|g'_{u,o}|$

Figure A.23: *Coma:* $B'_{2,r} = 0$, $B'_{2,i} = -8\ \mu\text{m}$

PSF extraction

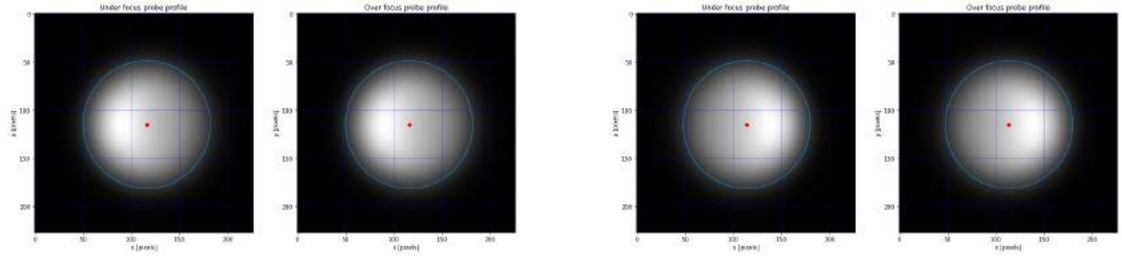

(a) (b)

Figure A.24: Extracted PSFs $|g_{u,o}|$ from the images in figure (A.20a) on the left and (A.21a) on the right.

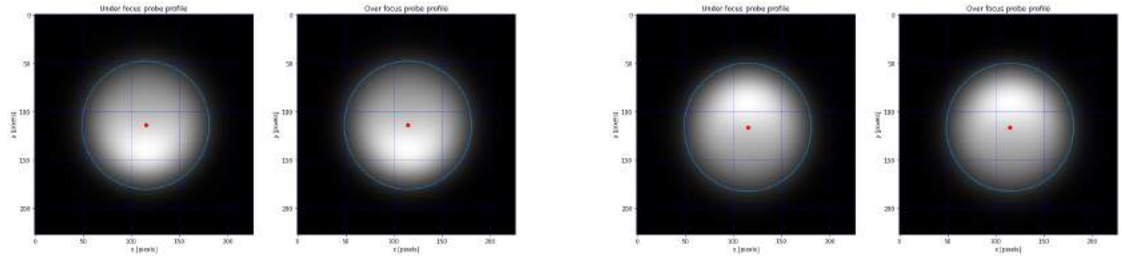

(a) (b)

Figure A.25: *Extracted PSFs $|g_{u,o}|$ from the images in figure (A.22a) on the left and (A.23a) on the right.*

Retrieved aberration coefficients

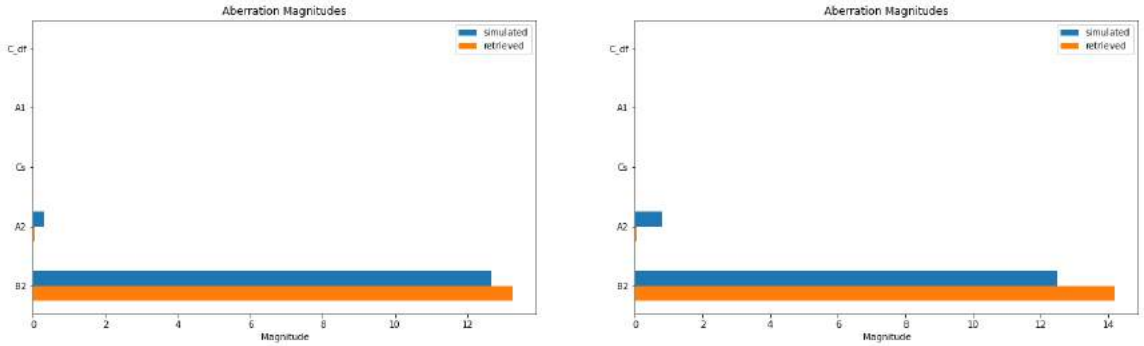

(a) $B'_{2,r} = 8\ \mu\text{m}$, $B'_{2,i} = 0$ (b) $B'_{2,r} = -8\ \mu\text{m}$, $B'_{2,i} = 0$

Figure A.26: *Coma, real*

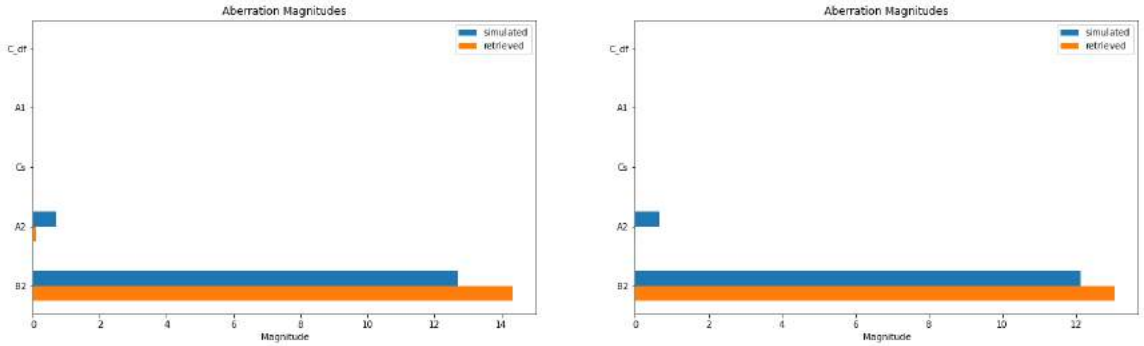

(a) $B'_{2,r} = 0$, $B'_{2,i} = 8\ \mu\text{m}$ (b) $B'_{2,r} = 0$, $B'_{2,i} = -8\ \mu\text{m}$

Figure A.27: *Coma, imaginary*

(s,Q) plot sample images

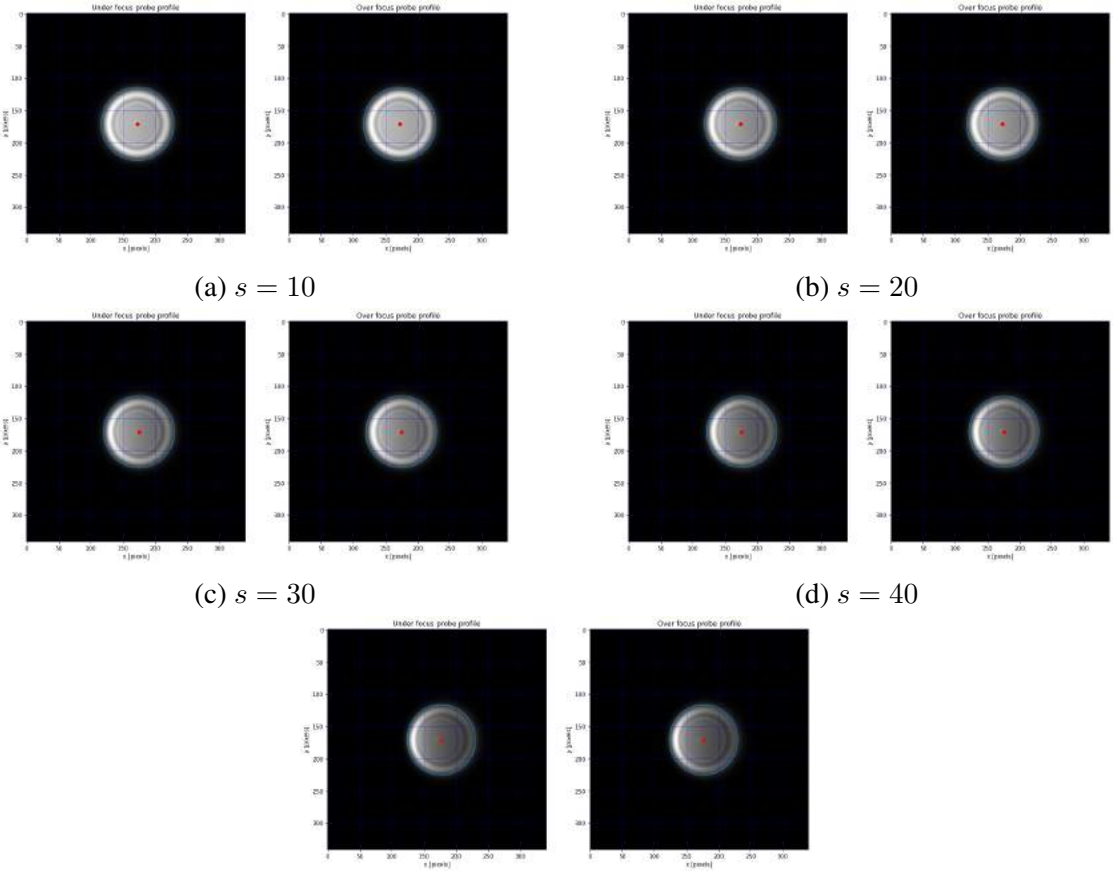

(a) $s = 10$ (b) $s = 20$

(c) $s = 30$ (d) $s = 40$

(e) $s = 50$

Figure A.28: *Simulated PSFs imitating spherical aberration with coefficients* $B'_{2,r,s} = sB'_{2,r,1}$, $B'_{2,r,1} = 0.2\ \mu\text{m}$*, see Table 4. The PSFs are shown for* $s = 10, 20, 30, 40, 50$.

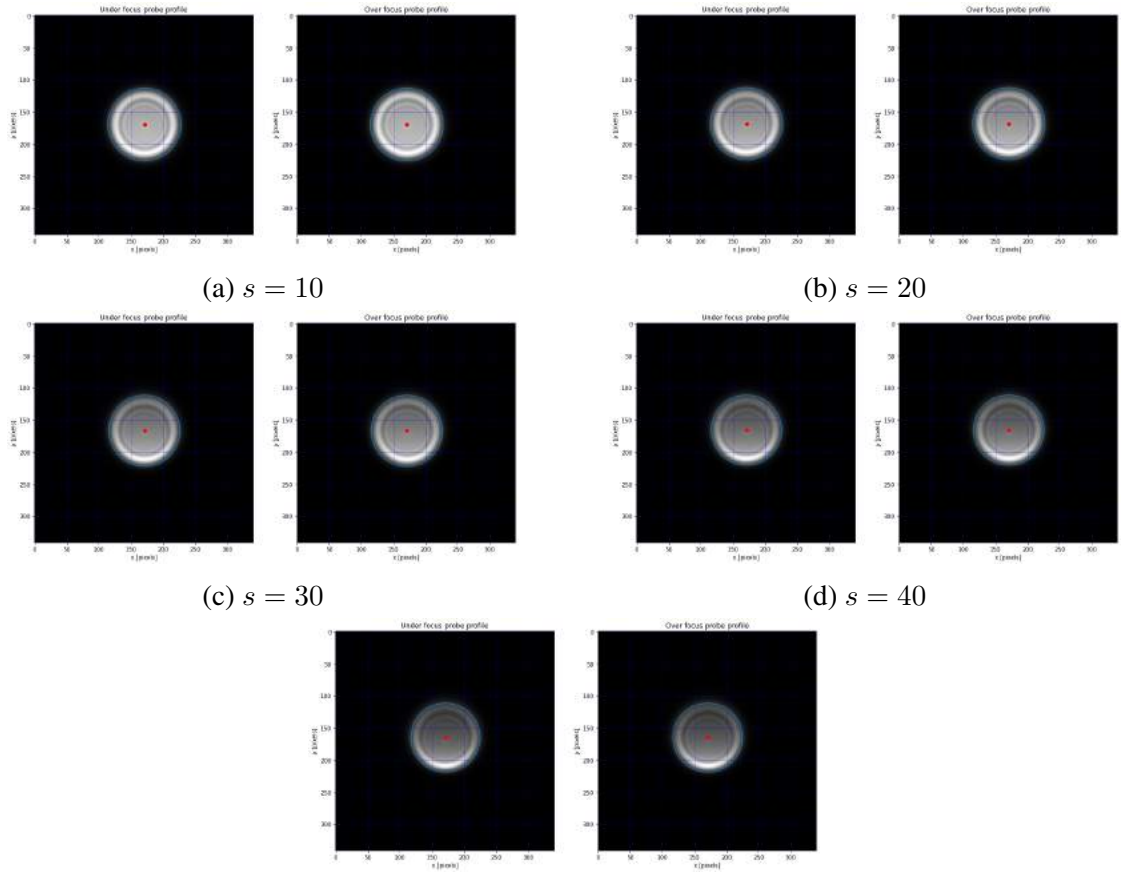

(a) $s = 10$

(b) $s = 20$

(c) $s = 30$

(d) $s = 40$

(e) $s = 50$

Figure A.29: *Simulated PSFs imitating spherical aberration with coefficients* $B'_{2,i,s} = sB'_{2,i,1}$, $B'_{2,i,1} = 0.2\ \mu\text{m}$, *see Table 4. The PSFs are shown for* $s = 10, 20, 30, 40, 50$.

Three-fold astigmatism

Through-focus series

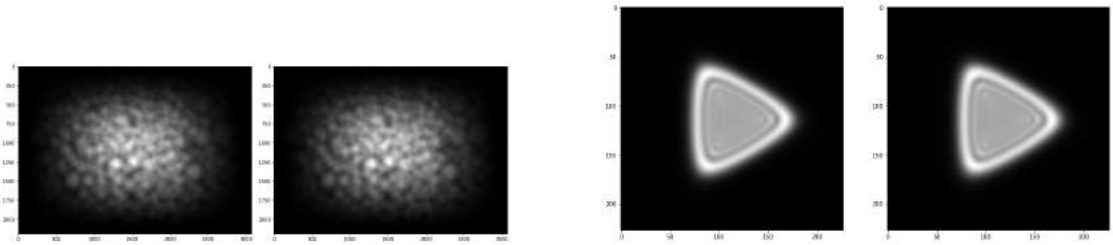

(a) *Simulated images* $h_{u,o}$ (b) *Simulated PSFs* $|g'_{u,o}|$

Figure A.30: *Three-fold astigmatism:* $A_{2,r} = 20\ \mu\text{m},\ A_{2,i} = 0$

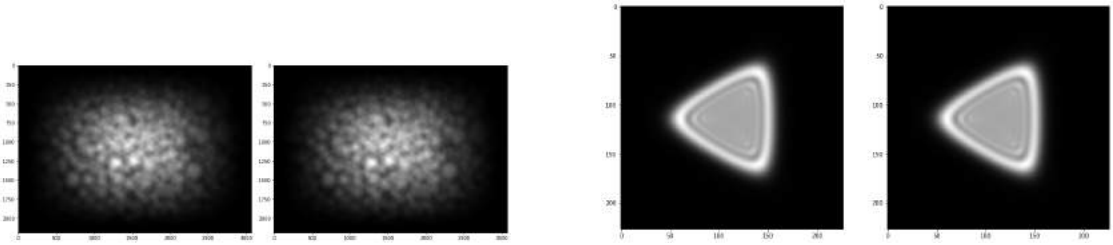

(a) *Simulated images* $h_{u,o}$ (b) *Simulated PSFs* $|g'_{u,o}|$

Figure A.31: *Three-fold astigmatism:* $A'_{2,r} = -20\ \mu\text{m},\ A'_{2,i} = 0$

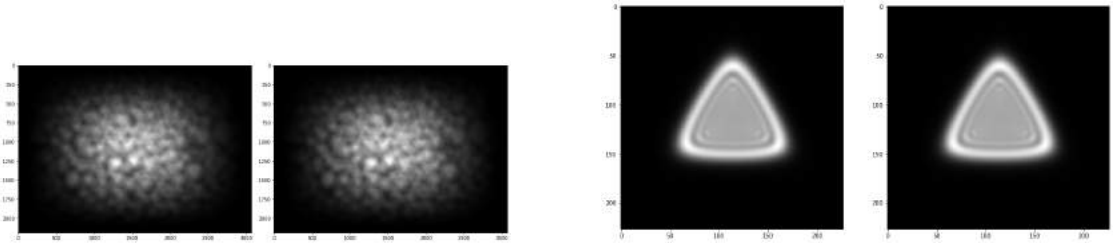

(a) *Simulated images* $h_{u,o}$ (b) *Simulated PSFs* $|g'_{u,o}|$

Figure A.32: *Three-fold astigmatism:* $A'_{2,r} = 0,\ A'_{2,i} = 20\ \mu\text{m}$

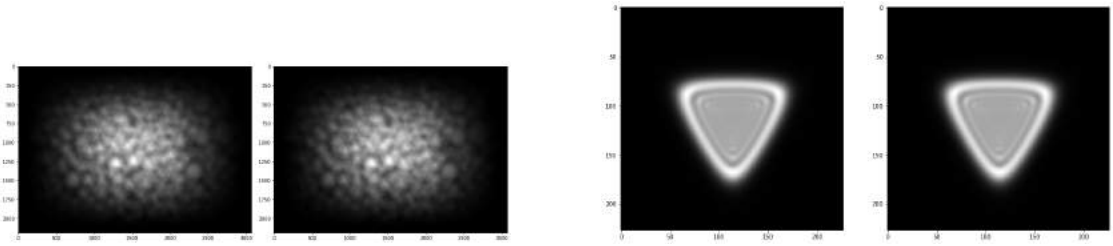

(a) *Simulated images* $h_{u,o}$ (b) *Simulated PSFs* $|g'_{u,o}|$

Figure A.33: *Three-fold astigmatism:* $A'_{2,r} = 0,\ A'_{2,i} = -20\ \mu\text{m}$

PSF extraction

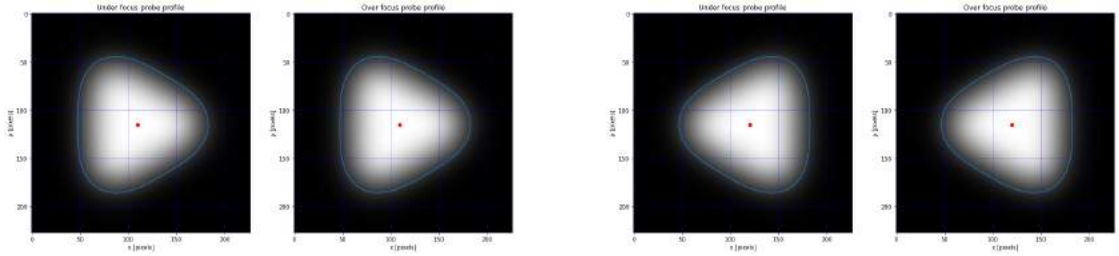

(a) (b)

Figure A.34: *Extracted PSFs $|g_{u,o}|$ from the images in figure (A.30a) on the left and (A.31a) on the right.*

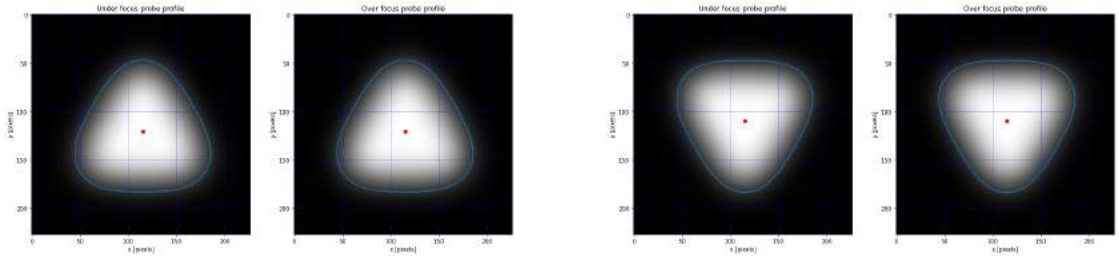

(a) (b)

Figure A.35: *Extracted PSFs $|g_{u,o}|$ from the images in figure (A.32a) on the left and (A.33a) on the right.*

Retrieved aberration coefficients

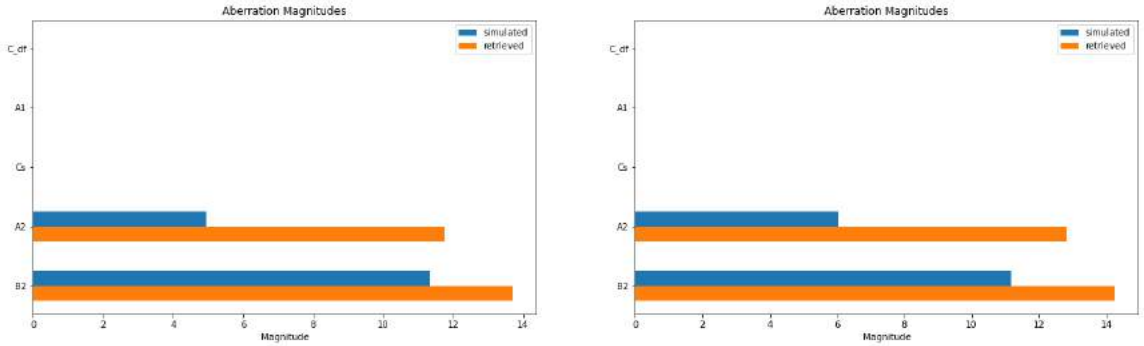

(a) $A_{2,r} = -20\ \mu\text{m}$, $A_{2,i} = 0$ (b) $A_{2,r} = 20\ \mu\text{m}$, $A_{2,i} = 0$

Figure A.36: *Three-fold astigmatism, real*

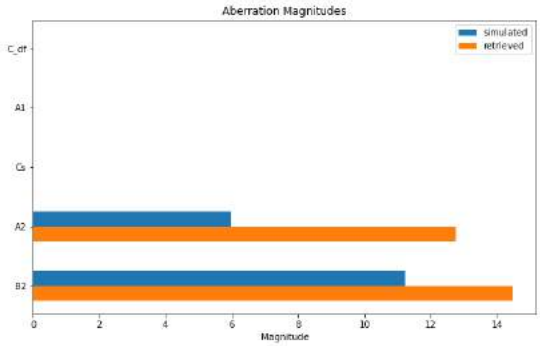

(a) $A_{2,r} = 0$, $A_{2,i} = 20$ μm

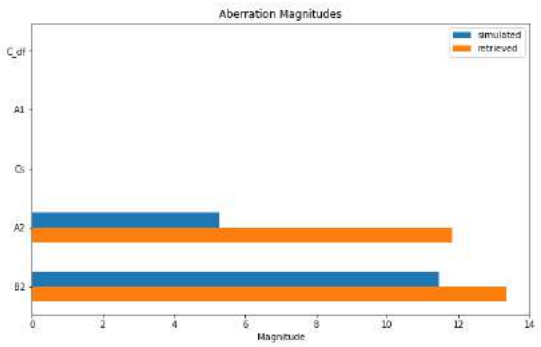

(b) $A_{2,r} = 0$, $A_{2,i} = -20$ μm

Figure A.37: *Three-fold astigmatism, imaginary*

(s,Q) plot sample images

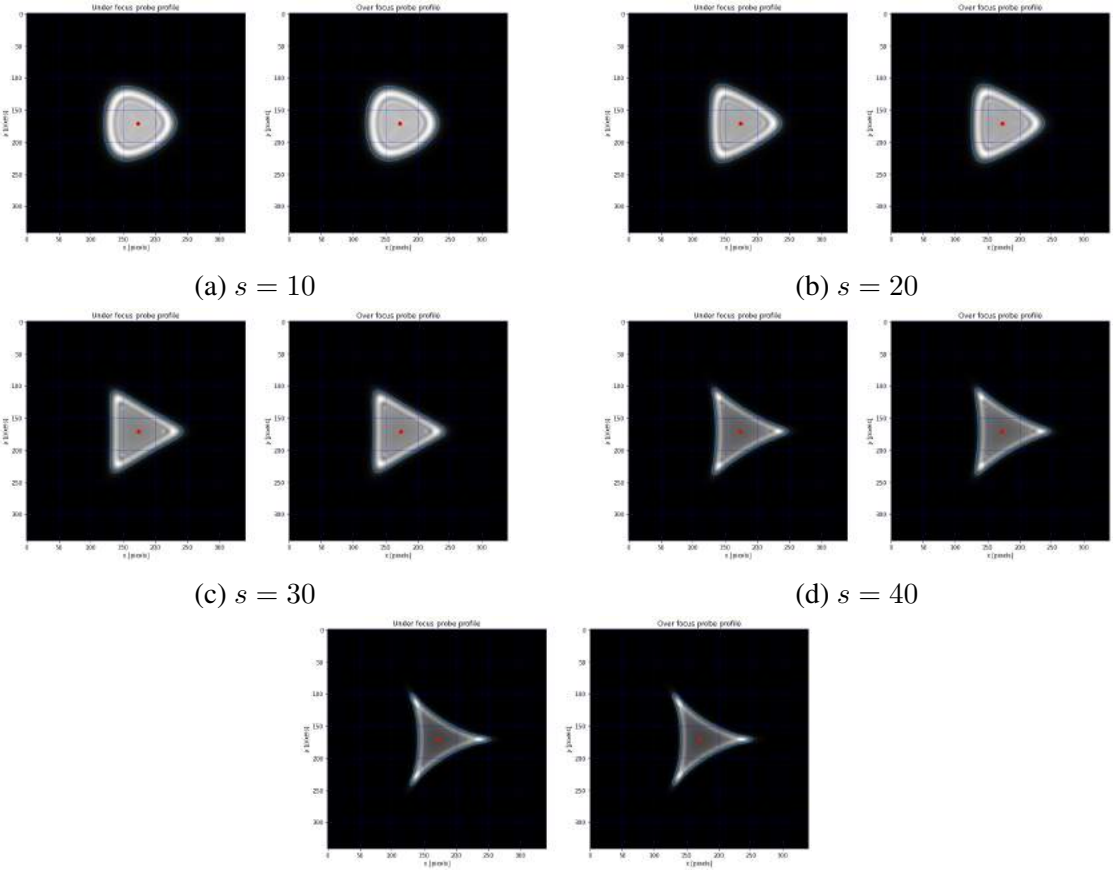

(a) $s = 10$

(b) $s = 20$

(c) $s = 30$

(d) $s = 40$

(e) $s = 50$

Figure A.38: *Simulated PSFs imitating spherical aberration with coefficients* $A'_{2,r,s} = sA'_{2,r,1}$, $A'_{2,r,1} = 1$ μm*, see Table 4. The PSFs are shown for* $s = 10, 20, 30, 40, 50$.

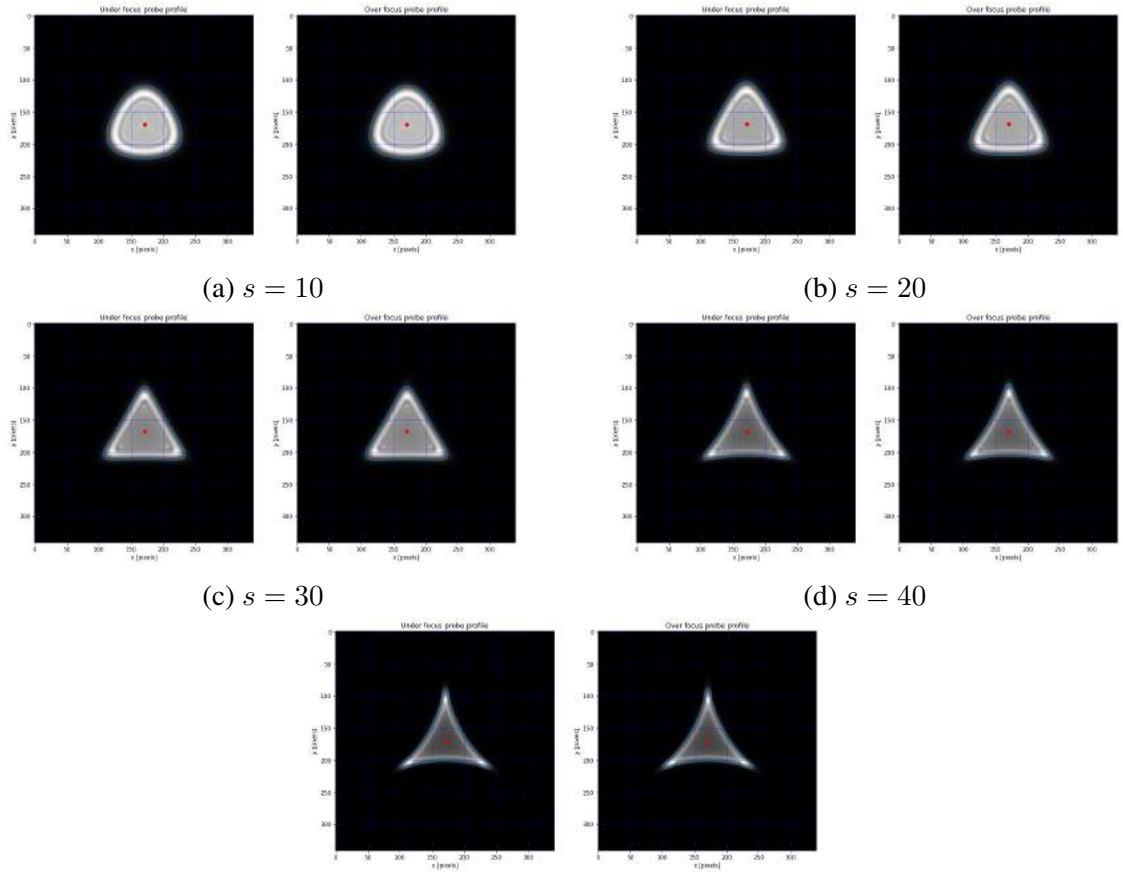

(a) $s = 10$

(b) $s = 20$

(c) $s = 30$

(d) $s = 40$

(e) $s = 50$

Figure A.39: *Simulated PSFs imitating spherical aberration with coefficients* $A'_{2,i,s} = sA'_{2,i,1}$, $A'_{2,i,1} = 1\ \mu\mathrm{m}$*, see Table 4. The PSFs are shown for* $s = 10, 20, 30, 40, 50$.